haematologica
Journal of the Ferrata Storti Foundation

Acid ceramidase controls proteasome inhibitor resistance and is a novel therapeutic target for the treatment of relapsed/refractory multiple myeloma

by Ryan T. Bishop, Tao Li, Praneeth Sudalagunta, Mostafa Nasr, Karl Nyman, Raghunandan R. Alugubelli, Mark Meads, Jeremy Frieling, Niveditha Nerlakanti, Marilena Tauro, Bin Fang, Steven Grant, John Koomen, Ariosto S. Silva, Kenneth H. Shain, and Conor C. Lynch

Received: April 23, 2024.
Accepted: November 27, 2024.

Citation: Ryan T. Bishop, Tao Li, Praneeth Sudalagunta, Mostafa Nasr, Karl Nyman, Raghunandan R. Alugubelli, Mark Meads, Jeremy Frieling, Niveditha Nerlakanti, Marilena Tauro, Bin Fang, Steven Grant, John Koomen, Ariosto S. Silva, Kenneth H. Shain, and Conor C. Lynch. Acid ceramidase controls proteasome inhibitor resistance and is a novel therapeutic target for the treatment of relapsed/refractory multiple myeloma.
Haematologica. 2024 Dec 5. doi: 10.3324/haematol.2024.285587 [Epub ahead of print]

Title

Acid ceramidase controls proteasome inhibitor resistance and is a novel therapeutic target for the treatment of relapsed / refractory multiple myeloma

Authors

Ryan T. Bishop[1], Tao Li[1], Praneeth Sudalagunta[2], Mostafa Nasr[1,3], Karl J. Nyman[1,3], Raghunandan R. Alugubelli[4], Mark Meads[1,5], Jeremy Frieling[1], Niveditha Nerlakanti[1,3], Marilena Tauro[1], Bin Fang[6], Steven Grant[7], John Koomen[6,8], Ariosto S. Silva[2], Kenneth H. Shain[1,8] and Conor C. Lynch[1]

Author Affiliations

[1] Department of Tumor Metastasis and Microenvironment., H. Lee Moffitt Cancer Center and Research Institute, Tampa, FL 33612, USA,

[2] Department of Metabolism and Physiology, H. Lee Moffitt Cancer Center and Research Institute, Tampa, FL 33612, USA

[3]Cancer Biology Ph.D. Program, University of South Florida, Tampa, FL, USA

[4] Collaborative Data Services Core, H. Lee Moffitt Cancer Center & Research Institute, Tampa, FL 33612, USA

[5]Department of Malignant Hematology, H. Lee Moffitt Cancer Center & Research Institute, Tampa, FL 33612, USA

[6]Chemical Biology & Molecular Medicine, H. Lee Moffitt Cancer Center & Research Institute, Tampa, FL 33612, USA

[7]Virginia Commonwealth University (VCU) Massey Cancer Center Richmond, VA, USA.

[8]Department of Molecular Oncology, H. Lee Moffitt Cancer Center & Research Institute, Tampa, FL 33612, USA

Author Contributions

R.T.B conceived, designed, performed, analyzed *in vitro*, *in vivo* and *ex vivo* studies, analyzed patient datasets and wrote the manuscript. T.L. performed *in vitro* experiments and assisted with animal studies. R.R.A. analyzed patient samples and acted as an honest broker for the PMRC MM patient dataset. P.R.S. analyzed and interpreted EMMA platform studies. M.N. performed patient data analysis and assisted with animal studies. J.F. and N.N. assisted with animal studies. K.N performed experiments and analysis. M.T performed an immunoblotting experiment. O.H. provided clinical samples. B.F. performed proteomic studies. M.M performed EMMA platform studies. S.G. provided materials and guidance. A.S. conceived and supervised clinical sample RNA-sequencing and EMMA platform analyses. J.K. supervised proteomic studies. K.H.S conceived and supervised patient sample and EMMA platform studies, interpreted and provided guidance on clinical data. C.C.L provided overall supervision and funding, and wrote the manuscript. All authors were involved in review and editing of the final manuscript.

Running title

ASAH1 controls PI-resistance in MM

Corresponding author

Correspondence to Conor C. Lynch - conor.lynch@moffitt.org

Data-sharing statement

All data is available from the corresponding author upon reasonable request. The PI-resistant C300R (derived from 5TGM1 murine MM) generated in this study are available from the lead contact (C.C.L) with a completed Materials Transfer Agreement.

Author conflicts of interest

J.K. received salary through a sponsored research agreement with Bristol Myers Squibb (BMS), unrelated to this study. K.H.S. reports honoraria from BMS, Janssen, Adaptive, Sanofi, and Takeda, and research funding to the institution from AbbVie and Karyopharm, outside the submitted work. KHS is also a member of advisory board for Sanofi, BMS, GlaxoSmithKline, Bristol Myers Squibb, Sanofi, Karyopharm, Janssen, and Amgen. The remaining authors have nothing to disclose.

Acknowledgements

The authors thank the patients at H. Lee Moffitt Cancer Center who provided clinical samples for our *ex vivo* assays as well as consented to access to their clinical data through the Total Cancer Care database. The authors also thank the Small Animal Imaging Laboratory, the Flow Cytometry, Tissue, Proteomics and Metabolomics, Biostatistics and Bioinformatics, and Analytical Microscopy Cores of the H. Lee Moffitt Cancer Center and Research Institute, an NCI designated Comprehensive Cancer Center (P30-CA076292), and the Comparative Medicine Department and the Electron Microscopy Core Facility of the University of South Florida (USF).

Funding

These studies were supported in part by R01-CA239214-01 (to C.C. Lynch) and R21-CA191981-01A1 (to C.C. Lynch), Physical Sciences in Oncology (PSOC) Grant 1U54CA193489-01A1 (to K.H.S., A.S.S., R.J.G, J.L.C., R.A.G), H. Lee Moffitt Cancer Center's Team Science Grant (A.S., K.H.S.), Miles for Moffitt Foundation (A.S.). Additionally, this work was supported by personal donations from The Pentecost Myeloma Research Center.

Abstract

Multiple myeloma (MM) patients are often refractory to targeted therapies including proteasome inhibitors (PIs). Here, analysis of RNA sequencing data derived from 672 patients with newly diagnosed or relapsed/refractory disease identified the acid ceramidase, ASAH1, as a key regulator of PI resistance. Genetic or pharmacological blockade of ASAH1 remarkably restored PI sensitivity and protected mice from resistant MM progression *in vivo*. Mechanistically, ASAH1 depletion of ceramide promoted SET inhibition of PP2A phosphatase activity thus facilitating the increased expression and activity of the pro-survival proteins, MCL-1, and BCL-2. We corroborated these findings in human MM datasets, and in *ex vivo* patient MM cells. These preclinical studies suggest that ASAH1 may be a potential therapeutic target for the treatment of relapsed/refractory MM (RRMM).

Introduction

Multiple myeloma (MM) is a clonal plasma cell malignancy in which the colonization and expansion of malignant clones in the bone marrow results in osteolysis, hypercalcemia, renal insufficiency, anemia and immunosuppression [1, 2]. Preclinical and clinical studies into the defining genetic and molecular alterations that drive MM pathophysiology, such as bone marrow microenvironment and ubiquitin-proteasome system (UPS) dependency have led to the development of numerous therapies to target MM-specific vulnerabilities. In particular, the introduction of proteasome inhibitors (PIs) such as bortezomib and carfilzomib, immunomodulatory drugs (IMiDs), and more recently selective inhibitors of nuclear export (SINEs), and cellular and non-cellular immunotherapies have significantly enhanced MM patient survival rates[3]. However, MM remains incurable, and relapsed/refractory MM (RRMM), defined primarily as progressive disease on treatment within 60 days of a given therapy[4, 5] occurs frequently leading to the patient's demise. Thus, identifying the mechanisms governing resistance can yield effective therapies for the treatment of RRMM.

Alterations in the cellular and molecular composition of the MM microenvironment as well as the development of acquired resistance mechanisms drive RRMM evolution. Typically, these mechanisms collectively enhance activation and or expression of pathways essential to RRMM proliferation (e.g., RAS/MAPK, NFκB, PI3K/AKT, JAK/STAT, MYC)[6-9] and/or survival (e.g., BCL-2 family members; BCL-2, MCL-1, BCL-xL, BCL-w, and BFL-1)[10-12]. Identification of resistance mechanisms can lead to the development of novel targeted therapies. An example being the recent FDA approved BCL-2 inhibitor, venetoclax. However, elevated MCL-1 levels can lead to venetoclax resistance in MM[13]. Therefore, therapies that can target upstream processes that regulate these pathways may exhibit superior efficacy or provide additional benefits when given in combination. In this regard, sphingolipid metabolism has been associated with increased pro-survival signaling that in turn has pathogenic implications for several malignancies including MM[14].

Sphingolipid metabolism largely involves regulating the balance between intracellular ceramide levels and conversion of ceramide to products such as sphingosine 1-phosphate (S1-P). Ceramides are fatty acid chains that can vary in length through the addition of carbon moieties and are critical for cell viability. For example, ceramide accumulation, specifically C2 or C6, induces cell cycle arrest in malignant cells whereas increases in C16 or C18 promote autophagic and apoptotic cell death through JNK and PKC [15, 16]. Notably, RRMM cells have significantly lower levels of ceramide compared to newly diagnosed drug naïve patients[17]. In contrast, the ceramide product, S1-P is regarded as a pro-tumorigenic sphingolipid. S1-P is

generated following ceramidase-mediated hydrolysis of ceramides into sphingosines that are subsequently phosphorylated by sphingosine kinases types 1 and 2 (SPHK1/2)[18]. S1-P has been shown to elicit pro-survival signaling through multiple effectors including but not limited to Myc and STAT3 [19-23].

Herein, we analyzed RNA sequencing data from the Pentecost Myeloma Research Center (PMRC) at Moffitt derived from newly diagnosed (NDMM), early relapsed/refractory (ERMM) and late relapsed/refractory MM (LRMM) patients and identified that increased expression of sphingolipid metabolism genes was significantly associated with relapsed/refractory disease. Specifically, this increase correlates with higher expression of the acid ceramidase, ASAH1, a hydrolase located in acidic lysosomes that converts pro-apoptotic ceramides into pro-survival S1-P. Notably, ASAH1 expression was found to be significantly upregulated in patients treated with any proteasome inhibitor containing regimen and predicted poorer overall survival when patients were treated with PI-containing regimens. Here, we delineate a causal role for ASAH1 in PI-resistance that has not previously been defined.

Materials and Methods

Patient Data

We investigated the expression of sphingolipid metabolism genes in cancer cells of 672 MM patients. Samples were taken from pre-treatment newly diagnosed multiple myeloma (NDMM, n=187), early relapsed/refractory MM (ERMM, 1-3 prior lines of therapy, n=303) or late relapsed/refractory MM (LRMM, >3 prior lines of therapy, n=182). Investigators obtained signed informed consent from all patients who were enrolled in the clinical trials/protocols MCC14745, MCC14690, and MCC18608 conducted at the H. Lee Moffitt Cancer Center and Research Institute, as approved by the Institutional Review Board. To this end, patient samples were used in accordance with the Declaration of Helsinki, International Ethical Guidelines for Biomedical Research Involving Human Subjects (CIOMS), Belmont Report, and U.S. Common Rule. The medical records were deidentified, and only the following clinically relevant information was reviewed: (A) patients' survival, (B) the treatment administered (therapeutic agents, doses, and schedule) prior to biopsy, (C) cytogenetics. RNA-seq data was normalized by Z-score. Patients were considered resistant to a treatment if patients had progressed on or within 90 days of a given treatment. PI resistance includes resistance to bortezomib, carfilzomib, oprozomib or marizomib. IMiD resistance includes resistance to thalidomide, lenalidomide or pomalidomide. Chemo resistance includes resistance to combinations of etoposide, vincristine, doxorubicin, and cyclophosphamide. Anti-CD38 resistance includes resistance to daratumumab or

isatuximumab. All MM patients were clustered using clustergrammer (version 2.0) based on expression 30 genes (WP_Sphingolipid Metabolism) or SET/ASAH1/MCL1/BCL2. Kaplan-Meier survival analyses for clusters and individual genes was performed using Prism.

Animal Studies

All animal experiments were done with University of South Florida (Tampa, FL) Institutional Animal Care and Use Committee approval (CCL; #7356R). Male and female 6-week-old immunodeficient mice NOD-SCIDγ (NSG) mice were divided into tumor naïve or tumor bearing mice (25/group). For the ceranib-2/bortezomib combination study PSR-RFP MM cells were injected ($5x10^6$ cells/100 µl PBS) by the tail vein inoculation. Tumors were allowed to establish and grown until RFP detection (Perkin Elmer IVIS Lumina) in the long bones (Day 28) and then divided in to 4 groups. Mice were treated with either vehicle, an induction dose of ceranib-2 (50mg/kg, 5xweek), BTZ (0.5mg/kg, 2xweek) or combination treatment. After one week, ceranib-2 was dropped to a maintenance dose (5mg/kg, 5xweekly). For the ASAH1-knockdown study, PSR-CTRL-RFP, or PSR-$ASAH1^{KD}$-RFP cells ($5x10^6$cells/100 µl PBS) or PBS (100 µl) were inoculated into mice via tail vein injection. Bortezomib treatment (0.5mg/kg, 2xweekly) was initiated after detection of serum IgE (Day 21) and followed clinical treatment schedules (2 weeks on/1 week off) until Day 63 when first mice reached endpoint of hind-limb paralysis. The study was terminated by CO_2 inhalation and cervical dislocation. Tibiae were excised and soft tissue removed for X-ray, histological and flow cytometric analyses.

Additional methods can be found in the supplementary

Results

Sphingolipid metabolism and ASAH1 are elevated in RRMM and predicts clinical outcome in RRMM patients

A number of oncogenic drivers of MM have been identified but recently there has been a shift towards understanding how metabolic processes can contribute to MM progression and resistance. Sphingolipid metabolism in particular has been associated with increased pro-survival signaling that in turn has pathogenic implications. Less is known regarding sphingolipid metabolism in RRMM. To that end, we leveraged RNA sequencing data from the Pentecost Myeloma Research Center (PMRC) at Moffitt that is composed of MM cells derived from newly diagnosed (NDMM; treatment naïve, n=187), early relapsed/refractory (ERMM; 1-3 lines of therapy, n=303) and late relapsed/refractory MM (LRMM; >3 lines of therapy n=182) patients.

We next assessed the expression of 30 genes involved in sphingolipid metabolism across this dataset. (**Supp Fig. 1a-b, Supp Table. 1**). Our analyses revealed that sphingolipid metabolism genes have significantly higher expression in RRMM (**Fig. 1a**). Hierarchical clustering analysis revealed two distinct clusters (Sphingo^{Low} and Sphingo^{High}), with the proportion of Sphingo^{High} patients increasing from NDMM to LRMM (**Supp Fig. 2a**). Notably, Sphingo^{High} patients exhibit significantly shorter overall survival times compared to Sphingo^{Low} patients, and this was particularly evident in RRMM (ERMM and LRMM patients combined, **Fig. 1b**, **Supp Fig. 2b**). Ceramides are the central sphingolipids from which multiple sphingolipid species are derived (**Supp Fig. 1b**). Our analysis revealed that the acid ceramidase (ASAH1) was significantly elevated in ERMM and LRMM patients compared to NDMM (**Fig. 1c**). We also noted a reduction in total ceramides in drug-resistant MM cell lines compared to their drug sensitive isogenic counterparts (**Fig. 1d)** and increased levels of S1-P (**Fig. 1d**), consistent with previously published reports[17]. These data indicate enhanced conversion of ceramide into S1-P in relapsed/refractory cells. Notably, of the enzymes involved in ceramide conversion to S1-P, only ASAH1 and sphingosine kinase-1 (SPHK1) were significantly upregulated in both ERMM and LRMM (**Supp Fig. 2c**). We next examined whether these genes were associated with resistance to standard of care therapies. While SPHK1 showed no significant association with any particular standard of care therapy, ASAH1 was significantly enriched in RRMM patients who were resistant to any proteasome inhibitor containing regimen (**Fig. 1e**). Of note, ASAH1 was not significantly associated with any cytogenetic risk groups (**Supp Fig. 2d**). Further, in the PMRC cohort, we found that high ASAH1 expression (>NDMM median z-score) in relapsed/refractory patients (regardless of any prior treatment) correlated with a worse overall survival (>2-fold survival reduction) when those patients specifically received a PI-containing regimen compared to those that did not (**Supp Fig 2e**). We further confirmed this correlation by interrogating patient data from the Multiple Myeloma Research Foundation (MMRF) CoMMpass trial (NCT0145429 - IA16). Analyses showed that newly diagnosed patients expressing high levels of ASAH1 mRNA (ASAH1^{High}, n= 385) had significantly shorter duration of response (503 days vs 804 days), progression free survival (1053 vs 1397 days) and overall survival (2183 days vs. not reached) compared to patients with low ASAH1 expression (ASAH1^{Low}, n=385) (**Supp Fig. 2e**). Importantly, 73.6% of these patients received PI-based regimens as first line therapy (*MMRIA16*). We further confirmed that established human PI-resistant MM cell lines[24-26] and a PI-resistant derivative of 5TGM1 (5TGM1-C300R) generated in-house exhibited elevated ASAH1 at the protein level in addition to elevated activity, as measured via RBM14C12 assay, compared to their isogenic parental controls (**Fig. 1f**; **Supp Fig. 2g** and **Supp Fig. 3**). Taken

together, these data establish ASAH1 as potentially playing a key role in mediating PI-resistance in RRMM specifically.

ASAH1 is a potential therapeutic target for RRMM

To determine if ASAH1 was playing a causal role in promoting the RRMM resistance, we first generated several ASAH1 knockdown PI-resistant MM cell lines using three independent shRNA constructs to reduce protein expression and subsequently activity down to levels comparable with PI-sensitive cells (**Supp Fig. 4a-b**). The two most effective constructs (PSR ASAH1 KD1 and KD3) were chosen for downstream analyses. SHRNA-mediated knockdown of ASAH1 expression in PI-resistant MM cell lines (**Supp Fig. 4a-b**) led to a modest yet significant decrease in MM cell growth over 48-72 hours *in vitro* (**Fig. 2a**; **Supp Fig. 4c**). We then focused on the feasibility of pharmacological ASAH1 inhibition. Notably, several ASAH1 targeted inhibitors have been developed given the role of the ceramidase in non-malignant pathologies such as Alzheimer's disease [27-33]. Of the available inhibitors, we found ceranib-2 to be the most effective (**Fig. 2b**; **Supp Fig 4d**). Importantly, it has also been characterized *in vivo* showing no signs of overt toxicity [31] thus we moved forward with this reagent. Subsequently, we observed that ceranib-2 reduced PI-resistant cell survival to significantly lower levels compared to PI-sensitive cells using six independent isogenic cell line series (IC_{50} range of 0.6-5.5 μM vs 0.2-1.6 μM for PI-sensitive or PI-resistant MM, respectively) after 72 hours of treatment (**Fig. 2c**). To test whether pharmacological inhibition of ASAH1 with ceranib-2 was effective for the treatment of PI-resistant MM *in vivo,* PI-resistant PSR[25, 26] expressing red fluorescent protein (PSR^{RFP}) were tail-vein injected into NSG mice. To better mimic late-stage disease, we allowed PSR^{RFP} cells to home to and colonize the bone and initiated treatments 30 days post inoculation following detection of serum IgE (day 21) and RFP signal in the hindlimbs (day 28). At day 30, mice were divided into three groups and treated with vehicle, 5 mg/kg ceranib-2 five times a week [31] or 0.5 mg/kg bortezomib twice weekly (approximating the clinical schedule and dose of 1.3mg/m^2). Longitudinal RFP imaging revealed ceranib-2 treatment significantly reduced growth of PI-resistant MM cells compared to vehicle and bortezomib treated controls (**Fig 2d-e**), as evidenced by a 34.5% and 38.4% reduction in Total Radiant Efficiency at day 63 compared to vehicle- and bortezomib-treated mice, respectively (**Supp Fig 5a**). Similar results were obtained by *ex vivo* RFP FACS analysis (**Supp Fig. 5b**), which demonstrated ceranib-2 treated mice had a 42.53% and a 58.14% reduction in the number of RFP% MM cells in the bone marrow at end point, compared to vehicle- and bortezomib-treated mice respectively. This reduction in tumor burden led to a significant 1.25- and 1.17-fold increase in median overall survival time of the

ceranib-2 treated mice compared to vehicle and bortezomib treated controls, respectively (**Fig. 2f**). As expected, bortezomib treatment had no effect on overall survival in PI-resistant MM compared to vehicle-treated mice (**Fig. 2d-e**).

Given the clinical significance of MM on bone destruction, we also examined the impact of ceranib-2 treatment on MM induced bone disease and observed a significant reduction in, cortical osteolytic lesions (**Supp Fig. 6a**), trabecular bone destruction (**Supp Fig. 6b and d**) and in the number of TRAcP+ osteoclasts (**Supp Fig. 6c**) in ceranib-2 treated mice compared to vehicle-treated controls. Taken together, these data point to ASAH1 inhibition as a viable therapeutic target for the treatment of RRMM and the associated bone disease that leads to fractures and other complications in patients.

ASAH1 inhibition alters sphingolipid levels leading to loss of anti-apoptotic protein expression and activity

We next queried the potential mechanisms through which ASAH1 might contribute to treatment resistance using gene-set enrichment analysis (GSEA). $ASAH1^{High}$ patients displayed upregulation of gene signatures involved in metabolism of lipids and sphingolipids as might be expected, and also regulation of apoptosis (**Fig. 3a**). Studies have implicated ASAH1 and sphingolipid metabolism in the expression and activation of pro-survival proteins such as MCL-1 and BCL-2 [16, 34]. Independent analysis of the CoMMpass and PMRC datasets revealed that $ASAH1^{High}$ patients had significantly increased levels of anti-apoptotic MCL-1 and BCL-2 mRNA (**Fig. 3b, Supp Fig. 7a**), with MCL-1, but not BCL-2 expression increasing in RRMM (**Supp Fig 7b**). Consistent with our patient data thus far, we observed that PI-resistant MM cell lines have elevated levels of ASAH1, and increased levels of total and phosphorylated MCL-1/BCL-2 compared to parental PI-sensitive MM cell lines (**Fig. 3c, Supp Fig. 7c-d**). In ASAH1 knockdown cell lines, we also observed reduced expression of both the total and phosphorylated forms of MCL-1 and BCL-2. In agreement, we observed that treatment of PI-resistant MM with ceranib-2 reduces MCL-1 and BCL-2 protein levels (**Fig. 3d, Supp Fig. 8a-b**) combined with an induction of apoptosis (**Supp Fig. 8c**).

Since ASAH1 has been reported to hydrolyze ceramides into sphingosine for conversion to S1-P by SPHKs, we assessed the levels of ceramide and S1-P following ASAH1 inhibition. As expected, both $ASAH1^{KD}$ and treatment with ceranib-2 enhanced levels of total ceramides in PI-resistant cells with a concurrent reduction in intracellular S1-P (**Fig. 3e**). In *ex vivo* bone marrow supernatants derived from our *in vivo* studies (**Fig. 2),** we also observed a complete loss of S1-P in ceranib-2 treated mice (**Fig 3e**).

To test if loss of S-1P or the accumulation of ceramides was responsible for changes in anti-apoptotic protein levels, we treated PI-resistant MM cells with the SPHK1/2 inhibitor, SKI-178 and noted no effect on anti-apoptotic protein levels (**Fig. 3f, Supp Fig 8d**). However, addition of exogenous ceramide reduced both MCL-1 and BCL-2 levels in PI-resistant MM (**Fig 3f, Supp Fig 8d**). Taken together, our data indicates that ASAH1 controls PI-resistant cell viability in response to PIs through degradation of ceramide levels to maintain high levels of active anti-apoptotic proteins.

ASAH1 inhibition restores sensitivity to PIs *in vitro* and *in vivo*

As ASAH1 inhibition reduces both MCL-1 and BCL-2 expression, and given their involvement in PI resistance, we investigated whether ASAH1 inhibition would restore sensitivity to PI treatment. To this end, treatment of control PI-resistant MM cells with BTZ had, as expected, no effect on cell viability, however, we noted ASAH1^{KD} cells were more sensitive to BTZ treatment at a level that was comparable to their PI-sensitive counterparts (**Fig. 4a**, **Supp Fig. 9a**). Supporting this finding, PI-resistant cells exposed to combination treatment of ceranib-2 and CFZ or BTZ displayed high levels of synergy and MM cell cytotoxicity (**Fig. 4b, Supp 9b**). Next, we asked whether resensitization could be recapitulated *in vivo*. We selected the most efficient shRNA-mediated knockdown (PSR KD1, **Supp Fig. 4a-b**) for *in vivo* studies. Control or ASAH1^{KD} PSR cells were inoculated into NSG mice and allowed to colonize the skeleton. Once serum IgE levels (a systemic marker of PSR growth) were detected (~ Day 21 post inoculation), treatment with BTZ or vehicle was initiated following clinical dosing and scheduling (twice weekly, three days apart) and continued until day 60 (**Fig. 4c**). Only BTZ-treated ASAH1^{KD} cells exhibited reduced MM growth *in vivo* compared to vehicle-treated CTRL mice, as quantified by serum longitudinal IgE. No significant effects on tumor growth were observed in vehicle-treated ASAH1 ^{KD} or BTZ-treated CTRL groups compared to vehicle-treated CTRL group (**Fig. 4d**). At study endpoint, we confirmed by flow-cytometry that only BTZ-treated ASAH1^{KD} treated mice had significantly less (59.89% less) HLA+ MM cells present in the long bones compared to vehicle treated CTRL group (**Fig. 4e**). Further, both vehicle- and BTZ-treated ASAH1^{KD} had significantly fewer MCL-1+ and BCL-2+ MM cells *ex vivo* compared to vehicle-treated CTRL cells (**Supp Fig. 9c, Fig. 4f**)). These data further support our findings that inhibition of ASAH1 reduces anti-apoptotic protein expression and restores sensitivity to proteasome inhibitors.

Ceramide accumulation inhibits of SET resulting in enhanced PP2A activity

Mechanistically, we next interrogated how ASAH1 blockade directly impacted pro-survival protein activity. Of note, the anti-apoptotic activity and stability of MCL-1 and BCL-2 are regulated by phosphorylation events that are governed by numerous kinases and the phosphatase, PP2A. We therefore performed LC-MS/MS proteomics to assess global phosphorylation (STY) changes in wildtype and ASAH1^{KD} MM cells. Robust kinase activity inference (RoKAI) app analysis was used to infer which phosphatases were differentially activated or inhibited (**Fig. 5a**)[35]. We noted the activity of PP2A, which dephosphorylates both MCL-1 and BCL-2 increased following ASAH1 inhibition (**Fig 5a**). We next confirmed our *in-silico* results using a specific PP2A activity assay where we demonstrated that knockdown of ASAH1 significantly enhanced PP2A activity (**Fig 5b**). Moreover, we confirmed this observation through treatment with ceranib-2 or via the addition of exogenous ceramide and observed both approaches induce strong activation of PP2A. Underscoring the specificity of this effect, addition of okadaic acid, a PP2A specific inhibitor, completely abolished the effects of ASAH1 knockdown, ceranib-2, and ceramide treatment on PP2A activity (**Fig. 5b)**.

Previous studies have identified PP2A as a ceramide activated phosphatase through direct ceramide binding to and inhibition of the endogenous inhibitor SET, also known as I2PP2A[36, 37]. Whilst knockdown of ASAH1 had no effect on SET expression (**Supp Fig. 10a**), siRNA-mediated knockdown of SET or pharmacological inhibition with FTY-720 [37], reduced both total and phosphorylated MCL-1 and BCL-2 expression (**Fig. 5c**, **Supp Fig. 10b-d**).

Further, knockdown of SET in PI-resistant MM cells resensitized these cells to BTZ treatment, whilst having no effect on cell viability in the absence of BTZ (**Fig. 5d**, **Supp Fig. 10e**). These data indicate that ASAH1 promotes high anti-apoptotic protein expression/activity through SET-mediated PP2A inhibition. Of note, in clinical specimens, the expression of ASAH1, SET, MCL1 and BCL2 increase significantly from NDMM to LRMM (**Fig. 5e**). Hierarchical clustering of all 672 PMRC MM samples based on these genes identify three distinct clusters **(Supp Fig. 7d**): cluster 1 (ASAH1/SET/MCL1^{Low} and BCL2^{Med}), cluster 2 (ASAH1/SET/MCL1^{High} and BCL2^{Low}) and cluster 3 (ASAH1/SET/MCL1/BCL2^{High}). RRMM patients belonging to cluster 2 or 3 treated specifically with a PI-containing regimen had significantly shorter overall survival compared to patients belonging to cluster 1 (385 and 583 vs 1866 days; **Supp Fig. 11a**) whereas no difference was observed in patients receiving a non-PI based regimen (**Supp Fig. 11b**). Taken together, these data demonstrate that RRMM cells sustain elevated BCL-2/MCL-1 expression in part through SET-mediated suppression of PP2A activity. Furthermore, specific inhibition of ASAH1 leads to intracellular ceramide accumulation, in turn activating PP2A and destabilizing MCL-1 and BCL-2 protein expression and activity (**Fig. 5f**).

Ceranib-2 synergizes with carfilzomib to resensitize patient-derived RRMM *ex vivo*

Thus far, our preliminary data indicate ASAH1 is a potent mediator of PI resistance in MM. To bolster this finding, we employed the novel *ex vivo* mathematical myeloma advisor (EMMA) platform[38, 39]. This technology allows for the testing of reagents as single therapies or in combination, on patient derived CD138+ selected MM cells cultured in the presence of patient-derived bone marrow stroma over a 6-day period using live cell imaging (**Fig 6a**). An area under the curve (AUC) up to 96 hours for each dose is calculated and results are displayed as a mean AUC. Importantly, and in keeping with our earlier findings, ceranib-2 is significantly more effective in targeted killing of RRMM patient cells than NDMM cells (**Fig 6b**). In fact, ceranib-2 is the only compound where the AUC was lower in the RRMM group as compared to the NDMM group (**Fig 6c**). Given our synergy findings (**Fig. 4**), we next focused on potential synergy within a cohort of NDMM and RRMM patients. We observed that the combination of ceranib-2 and carfilzomib was synergistic in 85.71% of RRMM patients (12/14 synergistic, 1/14 additive and 1/14 antagonistic) and 71.43% of NDMM patients (10/14 synergistic, 4/14 antagonistic; **Fig 6d-e, Supp Fig. 11c-d**). Further, we stratified all MM patients by their response to single agent CFZ *ex vivo* (CFZ sensitive: quartile 1; CFZ responsive: quartile 2 and 3; CFZ resistant: quartile 4). Here, we observed the highest degree of synergy in patients who were CFZ resistant (**Fig 6f**). Taken together these data indicate that addition of an ASAH1 targeting inhibitor to current PI treatments such as carfilzomib would deepen NDMM patient responses and resensitize RRMM patients to effective PI treatment.

Discussion

During the course of treatment, the vast majority of MM patients will receive proteasome inhibitor-based therapy. Whilst initially effective, patients typically become refractory and relapse. Many identified resistance mechanisms in MM converge on the activation of proliferative and anti-apoptotic pathways[13, 40, 41] and thus targeting of upstream signaling nodes may prove more efficacious. Sphingolipids have long been associated with MM. For example, patients with Gaucher disease have an increased risk of developing MM caused by a deficiency in glucocerebrosidase (GBA)[42]. Moreover, two of the best characterized sphingolipids, ceramides and S1-P have been shown to have opposing effects on survival in many healthy and malignant cells[16]. However, the role of sphingolipids and the pathways that control their metabolism have not been investigated in the context of RRMM. Here, we evaluated the expression of sphingolipid metabolism genes in 672 MM patients at different stages of disease

and identified acid ceramidase (ASAH1) as being associated with RRMM, specifically in the context of PI-resistance. We then demonstrated that both genetic and pharmacological inhibition of ASAH1 reduces cell viability in models of PI-resistant MM cells *in vitro* and *in vivo*. Excitingly, we also show that genetic/pharmacological inhibition of ASAH1 renders PI-resistant cells sensitive to PI *in vitro*, *in vivo,* and importantly, in isolated patient CD138+ MM cells *ex vivo*.

Analysis of a thirty sphingolipid metabolism gene signature revealed heightened expression in RRMM vs. NDMM patients. Of the twelve genes that were significantly upregulated in RRMM, eight controlled ceramide generation. Surprisingly, we found that proteasome inhibitor resistant cell lines had lower levels of total ceramides, but elevated levels of S1-P compared to their drug sensitive counterparts. In support of this observation, previous studies observed that RRMM patients have reduced levels of ceramides and elevated levels of sphingosine[17, 43]. Thus, we focused on the two significantly elevated genes involved in the conversion of ceramide to sphingosine and subsequent phosphorylation to S1-P i.e., ASAH1 and SPHK1 respectively. Whereas SPHK1 showed no significant association with any particular treatment regimen, ASAH1 showed significant upregulation in MM patients resistant to any regimen containing a proteasome inhibitor. Moreover, patients with elevated levels of ASAH1, regardless of prior therapy, had significantly poorer survival outcomes when treated with any PI-containing regimen but not non-PI regimen. Recently, it was shown that treatment with BTZ induces ceramide generation through ceramide synthases and the fatty acid elongase, ELOV6[43]. Thus, elevated ASAH1 may function to breakdown excess PI-generated ceramides and prevent apoptosis. Interestingly, ASAH1 was also elevated in RRMM patients resistant to anti-CD38 therapies thus ASAH1 inhibition may also be beneficial for patients treated with these non-cellular immunotherapies, however further studies are required to determine if this is the case, in addition to the precise molecular mechanisms at play.

Using a number of isogenic PI-resistant cell lines we demonstrate that ASAH1 is a therapeutic target for the treatment of PI-resistant MM. Both shRNA and pharmacological inhibition of ASAH1 with ceranib-2 reduced PI-resistant MM growth and resensitized cells to PIs through inhibition of the anti-apoptotic proteins MCL-1 and BCL-2 *in vitro* and *in vivo.* Inhibition of ASAH1 also led to an expected increase in total ceramides and a decrease in S1-P levels. Previous studies have shown that targeting of S1-P production through inhibition of SPHK1 and 2 reduces the expression of MCL1 but not BCL2 in acute myeloid leukemia and treatment naïve MM cell lines, respectively[44-46]. SPHK1/2 inhibition in PI-resistant MM did not alter anti-apoptotic protein expression, however treatment with exogenous ceramide or ceranib-2 led to loss of both proteins and reduced activity (**Fig. 3**). Importantly, ceranib-2, a commercially available ASAH1

inhibitor was effective for the treatment of RRMM *in vivo*, whereas bortezomib was not. Whilst these results are encouraging, previous PK/PD studies have demonstrated that ceranib-2 is rapidly cleared from plasma[31]. Therefore, development of more potent and longer lasting ceranib-2 derivatives is needed before ASAH1 inhibitors can be translated to the clinic. Altogether, these data further underscore the importance of sphingolipids in different stages of MM and that targeting a key upstream node of sphingolipid metabolism is a relevant therapeutic target for the treatment of RRMM.

While we have focused primarily on the effects of ASAH1 blockade in directly promoting RRMM cell cytotoxicity, we cannot rule out additional effects on the surrounding microenvironment. For example, previous reports have demonstrated that alterations in sphingolipids, particularly levels of S1-P, affect angiogenesis and reduce tumor growth *in vivo*[21, 47]. While we cannot fully rule out an effect of ceranib-2 on angiogenesis, our *in vivo* models were performed in established RRMM tumors and supported by our *in vitro* data which point to a MM-specific role of ASAH1 inhibition. Another important caveat is that our *in vivo* studies were performed in immunocompromised mice. NDMM and RRMM patients have demonstrated alterations of immune cells such as expansion of immune suppressive myeloid cells and exhausted γδT-cells and decreased CD4/CD8 T-cells in the bone marrow microenvironment[48]. Thus, a limitation of our study is the lack of syngeneic immunocompetent models as both ceramides and S1-P play roles in the immune system. Recently, it was demonstrated that ceramides/S1-P have opposing roles in the polarization of pro-inflammatory M1 macrophages and anti-inflammatory M2 macrophages, respectively[47, 49]. Our data demonstrate that ASAH1 upregulation is also associated with relapse to anti-CD38 therapies, including daratumumab and isatuximab (**Fig. 1h**). ASAH1-mediated degradation of ceramide and subsequent conversion to S1-P in MM cells may push bone marrow macrophages towards an M2-like state. These macrophages are generally believed to be anti-inflammatory, contributing towards an immune suppressed microenvironment and poor response to immunotherapies[50]. Further, accumulation of ceramide synthase-6 generated ceramides in ageing T-cells was demonstrated to induce mitophagy and limit anti-tumor immunity[51]. Similarly, S1-P reduces central memory T cell phenotype, expands immunosuppressive regulatory T cells (Tregs) and diminishes anti-tumor activity[52, 53]. Whilst the role of ASAH1 in individual immune cell subsets is unknown, future studies should further investigate how ASAH1 targeting therapies alter the MM immune microenvironment.

Mechanistically, our studies indicate that ASAH1 blockade leads to ceramide accumulation that in turn inhibits SET and thus enhances PP2A phosphatase activity. SET has

been designated an oncoprotein in several solid and hematological malignancies via; the regulation of histone and non-histone protein acetylation, regulation of the inhibitor of acetyltransferases (INHAT) complex, and the inhibition of the tumor suppressor PP2A[54-58]. Recently, it was discovered that ceramides induce PP2A activation by directly binding to and inhibiting SET[36, 59]. PP2A is cellular phosphatase that negatively regulates multiple pro-survival signaling pathways associated with cancer progression such as, ERK, Akt, JAK, β-catenin and c-Myc[60-63]. In drug naïve MM cell lines, it has been proposed that PP2A increases MCL-1 half-life and that inhibition with okadaic acid results in MM cell death by dephosphorylating Ser159/Thr163 on MCL1. Our data, however, indicate a role for PP2A-mediated dephosphorylation of MCL-1 Thr163 leading to loss of total protein, thus suggesting PP2A activation would be an ideal target for the treatment of RRMM. In support of this, it was shown in AML, pharmacological inhibition of ASAH1 lead to loss of phospho-MCL1 and total MCL-1, but not BCL-2 through an undescribed posttranslational mechanism[34]. In addition, we demonstrate that two subgroups of patients with high levels of ASAH1/SET/MCL-1 exist. One subgroup of patients has low levels of BCL-2 and one high. Both of these subgroups have significantly shorter overall survival times compared to ASAH1/SET/MCL-1low/BCL-2intermediate patients. Whilst this could suggest that BCL-2 expression may not be as important as MCL-1 to MM cell survival, several studies have demonstrated an additive or synergistic benefit of targeting both survival proteins[64, 65]. Furthermore, whilst we have demonstrated a role for ASAH1/SET/PP2A in regulating the expression anti-apoptotic proteins in RRMM, an alternative explanation is that depletion of ASAH1, rather than restoring sensitivity to PIs, activates an alternate pathway leads to apoptosis that is further enhanced by PIs. Total protein proteomics revealed changes in the unfolded protein response (UPR) and endoplasmic reticulum stress (ER) stress upon ASAH1 inhibition (data not shown), which are key pathways in MM pathobiology and could explain the enhanced apoptosis observed following ASAH1 inhibition. In other tumor types, ASAH1 expression was shown to alter numerous pathways to drive tumor growth and metastasis including NF□B, peroxisome biogenesis, and ROS production, neosis and autophagy [27, 34, 66-69]. Recently, it was shown that elevated ASAH1 levels were correlated with poor radiation response in prostate cancer patients. Moreover, the elevated ASAH1 expression was shown to be driven by enhanced activity of the transcription factor, c-Jun in prostate cancer cells. However, the mechanism through which ASAH1 prevents radiation induced apoptosis was not elucidated. Our study is the first to identify a mechanism through which ASAH1 protects tumor cells against PI-induced apoptosis and the same mechanism may be present in other solid malignancies or in response to other treatments such as anti-CD38 antibodies. Whilst these

ASAH1 regulated pathways may also contribute to PI resistance, our data herein show that ASAH1 control of phosphatase PP2A activity is a key mechanism involved in PI-resistance.

In conclusion, we have described a significant and a previously unknown role for ASAH1 in PI-resistance in MM. ASAH1 is not only elevated in PI-resistant MM patients, but its inhibition can also restore PI-sensitivity, through inactivation of SET and reduction of MCL1 and BCL2 expression and activity. These data provide strong rationale for the development of novel and potent inhibitors of ASAH1 activity, with favorable pharmacokinetic/dynamic profiles, in combination with PI for the treatment of RRMM.

References:

1. Kumar SK, Rajkumar V, Kyle RA, et al. Multiple myeloma. Nat Rev Dis Primers. 2017;3:17046.
2. Roodman GD. Pathogenesis of myeloma bone disease. J Cell Biochem. 2010;109(2):283-291.
3. Cowan AJ, Green DJ, Kwok M, et al. Diagnosis and Management of Multiple Myeloma: A Review. JAMA. 2022;327(5):464-477.
4. Rajkumar SV, Harousseau JL, Durie B, et al. Consensus recommendations for the uniform reporting of clinical trials: report of the International Myeloma Workshop Consensus Panel 1. Blood. 2011;117(18):4691-4695.
5. Sonneveld P. Management of multiple myeloma in the relapsed/refractory patient. Hematology Am Soc Hematol Educ Program. 2017;2017(1):508-517.
6. Hu J, Hu WX. Targeting signaling pathways in multiple myeloma: Pathogenesis and implication for treatments. Cancer Lett. 2018;414:214-221.
7. Jovanovic KK, Roche-Lestienne C, Ghobrial IM, Facon T, Quesnel B, Manier S. Targeting MYC in multiple myeloma. Leukemia. 2018;32(6):1295-1306.
8. Ghermezi M, Spektor TM, Berenson JR. The role of JAK inhibitors in multiple myeloma. Clin Adv Hematol Oncol. 2019;17(9):500-505.
9. Ramakrishnan V, Kumar S. PI3K/AKT/mTOR pathway in multiple myeloma: from basic biology to clinical promise. Leuk Lymphoma. 2018;59(11):2524-2534.
10. Oancea M, Mani A, Hussein MA, Almasan A. Apoptosis of multiple myeloma. Int J Hematol. 2004;80(3):224-231.
11. Inam S, Ross JA, Touzeau C, Moreau P, Kumar SK, Harrison SJ. Paving the way to precision medicine in multiple myeloma. Expert Rev Hematol. 2021;14(4):323-327.
12. Aksoy O, Lind J, Sunder-Plassmann V, Vallet S, Podar K. Bone marrow microenvironment- induced regulation of Bcl-2 family members in multiple myeloma (MM): Therapeutic implications. Cytokine. 2023;161:156062.
13. Punnoose EA, Leverson JD, Peale F, et al. Expression Profile of BCL-2, BCL-XL, and MCL-1 Predicts Pharmacological Response to the BCL-2 Selective Antagonist Venetoclax in Multiple Myeloma Models. Mol Cancer Ther. 2016;15(5):1132-1144.
14. Evangelisti C, Evangelisti C, Buontempo F, et al. Therapeutic potential of targeting sphingosine kinases and sphingosine 1-phosphate in hematological malignancies. Leukemia. 2016;30(11):2142-2151.
15. Sentelle RD, Senkal CE, Jiang W, et al. Ceramide targets autophagosomes to mitochondria and induces lethal mitophagy. Nat Chem Biol. 2012;8(10):831-838.
16. Young MM, Kester M, Wang HG. Sphingolipids: regulators of crosstalk between apoptosis and autophagy. J Lipid Res. 2013;54(1):5-19.
17. Mohamed A, Collins J, Jiang H, et al. Concurrent lipidomics and proteomics on malignant plasma cells from multiple myeloma patients: Probing the lipid metabolome. PLoS One. 2020;15(1):e0227455.
18. Hannun YA, Obeid LM. Sphingolipids and their metabolism in physiology and disease. Nat Rev Mol Cell Biol. 2018;19(3):175-191.
19. Wallington-Beddoe CT PJ, Tong D, Pitson SM, Bradstock KF, Bendall LJ. Sphingosine kinase 2 promotes acute lymphoblastic leukemia by enhancing MYC expression. Cancer Res. 2014;74(10):2803-2815.

20. Liang J, Nagahashi M, Kim EY, et al. Sphingosine-1-phosphate links persistent STAT3 activation, chronic intestinal inflammation, and development of colitis-associated cancer. Cancer Cell. 2013;23(1):107-120.
21. Visentin B, Vekich JA, Sibbald BJ, et al. Validation of an anti-sphingosine-1-phosphate antibody as a potential therapeutic in reducing growth, invasion, and angiogenesis in multiple tumor lineages. Cancer Cell. 2006;9(3):225-238.
22. Zhang L, Liu X, Zuo Z, Hao C, Ma Y. Sphingosine kinase 2 promotes colorectal cancer cell proliferation and invasion by enhancing MYC expression. Tumour Biol. 2016;37(6):8455-8460.
23. Ponnusamy S, Selvam SP, Mehrotra S, et al. Communication between host organism and cancer cells is transduced by systemic sphingosine kinase 1/sphingosine 1-phosphate signalling to regulate tumour metastasis. EMBO Mol Med. 2012;4(8):761-775.
24. Zhuang J, Shirazi F, Singh RK, et al. Ubiquitin-activating enzyme inhibition induces an unfolded protein response and overcomes drug resistance in myeloma. Blood. 2019;133(14):1572-1584.
25. Chen S, Dai Y, Pei XY, et al. CDK inhibitors upregulate BH3-only proteins to sensitize human myeloma cells to BH3 mimetic therapies. Cancer Res. 2012;72(16):4225-4237.
26. Chen S, Zhang Y, Zhou L, et al. A Bim-targeting strategy overcomes adaptive bortezomib resistance in myeloma through a novel link between autophagy and apoptosis. Blood. 2014;124(17):2687-2697.
27. Cheng JC, Bai A, Beckham TH, et al. Radiation-induced acid ceramidase confers prostate cancer resistance and tumor relapse. J Clin Invest. 2013;123(10):4344-4358.
28. Doan NB, Nguyen HS, Montoure A, et al. Acid ceramidase is a novel drug target for pediatric brain tumors. Oncotarget. 2017;8(15):24753-24761.
29. Pizzirani D, Bach A, Realini N, et al. Benzoxazolone carboxamides: potent and systemically active inhibitors of intracellular acid ceramidase. Angew Chem Int Ed Engl. 2015;54(2):485-489.
30. Vethakanraj HS, Sesurajan BP, Padmanaban VP, Jayaprakasam M, Murali S, Sekar AK. Anticancer effect of acid ceramidase inhibitor ceranib-2 in human breast cancer cell lines MCF-7, MDA MB-231 by the activation of SAPK/JNK, p38 MAPK apoptotic pathways, inhibition of the Akt pathway, downregulation of ERalpha. Anticancer Drugs. 2018;29(1):50-60.
31. Draper JM, Xia Z, Smith RA, Zhuang Y, Wang W, Smith CD. Discovery and Evaluation of Inhibitors of Human Ceramidase. Mol Cancer Ther. 2011;10(11):2052-2061.
32. Chavez JA, Holland WL, Bar J, Sandhoff K, Summers SA. Acid ceramidase overexpression prevents the inhibitory effects of saturated fatty acids on insulin signaling. J Biol Chem. 2005;280(20):20148-20153.
33. Bedia C, Casas J, Andrieu-Abadie N, Fabrias G, Levade T. Acid Ceramidase Expression Modulates the Sensitivity of A375 Melanoma Cells to Dacarbazine*. J Biol Chem. 2011;286(32):28200-28209.
34. Tan SF, Liu X, Fox TE, et al. Acid ceramidase is upregulated in AML and represents a novel therapeutic target. Oncotarget. 2016;7(50):83208-83222.

35. Yilmaz S, Ayati M, Schlatzer D, Cicek AE, Chance MR, Koyuturk M. Robust inference of kinase activity using functional networks. Nat Commun. 2021;12(1):1177.
36. De Palma RM, Parnham SR, Li Y, et al. The NMR-based characterization of the FTY720-SET complex reveals an alternative mechanism for the attenuation of the inhibitory SET-PP2A interaction. FASEB J. 2019;33(6):7647-7666.
37. Saddoughi SA, Gencer S, Peterson YK, et al. Sphingosine analogue drug FTY720 targets I2PP2A/SET and mediates lung tumour suppression via activation of PP2A-RIPK1-dependent necroptosis. EMBO Mol Med. 2013;5(1):105-121.
38. Silva A, Silva MC, Sudalagunta P, et al. An Ex Vivo Platform for the Prediction of Clinical Response in Multiple Myeloma. Cancer Res. 2017;77(12):3336-3351.
39. Sudalagunta P, Silva MC, Canevarolo RR, et al. A pharmacodynamic model of clinical synergy in multiple myeloma. EBioMedicine. 2020;54:102716.
40. Abdi J, Chen G, Chang H. Drug resistance in multiple myeloma: latest findings and new concepts on molecular mechanisms. Oncotarget. 2013;4(12):2186-2207.
41. Seiller C, Maiga S, Touzeau C, et al. Dual targeting of BCL2 and MCL1 rescues myeloma cells resistant to BCL2 and MCL1 inhibitors associated with the formation of BAX/BAK hetero-complexes. Cell Death Dis. 2020;11(5):316.
42. Barth BM, Shanmugavelandy SS, Tacelosky DM, Kester M, Morad SA, Cabot MC. Gaucher's disease and cancer: a sphingolipid perspective. Crit Rev Oncog. 2013;18(3):221-234.
43. Lipchick BC, Utley A, Han Z, et al. The fatty acid elongase ELOVL6 regulates bortezomib resistance in multiple myeloma. Blood Adv. 2021;5(7):1933-1946.
44. Hengst JA, Dick TE, Sharma A, et al. SKI-178: A Multitargeted Inhibitor of Sphingosine Kinase and Microtubule Dynamics Demonstrating Therapeutic Efficacy in Acute Myeloid Leukemia Models. Cancer Transl Med. 2017;3(4):109-121.
45. Venkata JK, An N, Stuart R, et al. Inhibition of sphingosine kinase 2 downregulates the expression of c-Myc and Mcl-1 and induces apoptosis in multiple myeloma. Blood. 2014;124(12):1915-1925.
46. Powell JA, Lewis AC, Zhu W, et al. Targeting sphingosine kinase 1 induces MCL1-dependent cell death in acute myeloid leukemia. Blood. 2017;129(6):771-782.
47. Weigert A, Tzieply N, von Knethen A, et al. Tumor cell apoptosis polarizes macrophages role of sphingosine-1-phosphate. Mol Biol Cell. 2007;18(10):3810-3819.
48. Yao L, Jayasinghe RG, Lee Bh, et al. Comprehensive Characterization of the Multiple Myeloma Immune Microenvironment Using Integrated scRNA-seq, CyTOF, and CITE-seq Analysis. Cancer Res Commun. 2022;2(10):1255-1265.
49. Sun H, Sun S, Chen G, et al. Ceramides and sphingosine-1-phosphate mediate the distinct effects of M1/M2-macrophage infusion on liver recovery after hepatectomy. Cell Death Dis. 2021;12(4):324.
50. Usmani SZ, Khan I, Chiu C, et al. Deep sustained response to daratumumab monotherapy associated with T-cell expansion in triple refractory myeloma. Exp Hematol Oncol. 2018;7:3.
51. Vaena S, Chakraborty P, Lee HG, et al. Aging-dependent mitochondrial dysfunction mediated by ceramide signaling inhibits antitumor T cell response. Cell Rep. 2021;35(5):109076.
52. Priceman SJ, Shen S, Wang L, et al. S1PR1 is crucial for accumulation of regulatory T cells in tumors via STAT3. Cell Rep. 2014;6(6):992-999.

53. Chakraborty P, Vaena SG, Thyagarajan K, et al. Pro-Survival Lipid Sphingosine-1-Phosphate Metabolically Programs T Cells to Limit Anti-tumor Activity. Cell Rep. 2019;28(7):1879-1893.e7.
54. von Lindern M, van Baal S, Wiegant J, Raap A, Hagemeijer A, Grosveld G. Can, a putative oncogene associated with myeloid leukemogenesis, may be activated by fusion of its 3' half to different genes: characterization of the set gene. Mol Cell Biol. 1992;12(8):3346-3355.
55. Adachi Y, Pavlakis GN, Copeland TD. Identification and characterization of SET, a nuclear phosphoprotein encoded by the translocation break point in acute undifferentiated leukemia. J Biol Chem. 1994;269(3):2258-2262.
56. Di Mambro A, Esposito MT. Thirty years of SET/TAF1beta/I2PP2A: from the identification of the biological functions to its implications in cancer and Alzheimer's disease. Biosci Rep. 2022;42(11):BSR20221280.
57. Seo SB, McNamara P, Heo S, Turner A, Lane WS, Chakravarti D. Regulation of histone acetylation and transcription by INHAT, a human cellular complex containing the set oncoprotein. Cell. 2001;104(1):119-130.
58. Seo SB, Macfarlan T, McNamara P, et al. Regulation of histone acetylation and transcription by nuclear protein pp32, a subunit of the INHAT complex. J Biol Chem. 2002;277(16):14005-14010.
59. Mukhopadhyay A, Saddoughi SA, Song P, et al. Direct interaction between the inhibitor 2 and ceramide via sphingolipid-protein binding is involved in the regulation of protein phosphatase 2A activity and signaling. FASEB J. 2009;23(3):751-763.
60. Arnold HK, Sears RC. A tumor suppressor role for PP2A-B56alpha through negative regulation of c-Myc and other key oncoproteins. Cancer Metastasis Rev. 2008;27(2):147-158.
61. Gotz J, Probst A, Mistl C, Nitsch RM, Ehler E. Distinct role of protein phosphatase 2A subunit Calpha in the regulation of E-cadherin and beta-catenin during development. Mech Dev. 2000;93(1-2):83-93.
62. Samanta AK, Chakraborty SN, Wang Y, et al. Jak2 inhibition deactivates Lyn kinase through the SET-PP2A-SHP1 pathway, causing apoptosis in drug-resistant cells from chronic myelogenous leukemia patients. Oncogene. 2009;28(14):1669-1681.
63. Resjo S, Goransson O, Harndahl L, Zolnierowicz S, Manganiello V, Degerman E. Protein phosphatase 2A is the main phosphatase involved in the regulation of protein kinase B in rat adipocytes. Cell Signal. 2002;14(3):231-238.
64. Carter BZ, Mak PY, Tao W, et al. Maximal Activation of Apoptosis Signaling by Cotargeting Antiapoptotic Proteins in BH3 Mimetic-Resistant AML and AML Stem Cells. Mol Cancer Ther. 2022;21(6):879-889.
65. Yi X, Sarkar A, Kismali G, et al. AMG-176, an Mcl-1 Antagonist, Shows Preclinical Efficacy in Chronic Lymphocytic Leukemia. Clin Cancer Res. 2020;26(14):3856-3867.
66. Tan SF, Dunton W, Liu X, et al. Acid ceramidase promotes drug resistance in acute myeloid leukemia through NF-kappaB-dependent P-glycoprotein upregulation. J Lipid Res. 2019;60(6):1078-1086.
67. White-Gilbertson S, Lu P, Norris JS, Voelkel-Johnson C. Genetic and pharmacological inhibition of acid ceramidase prevents asymmetric cell division by neosis. J Lipid Res. 2019;60(7):1225-1235.

68. Lai M, Amato R, La Rocca V, et al. Acid ceramidase controls apoptosis and increases autophagy in human melanoma cells treated with doxorubicin. Sci Rep. 2021;11(1):11221.
69. Malvi P, Janostiak R, Nagarajan A, Zhang X, Wajapeyee N. N-acylsphingosine amidohydrolase 1 promotes melanoma growth and metastasis by suppressing peroxisome biogenesis-induced ROS production. Mol Metab. 2021;48:101217.

Figure 1. Sphingolipid metabolism and ASAH1 are elevated in proteasome inhibitor-resistant multiple myeloma.

a. RNA-seq was performed on the Pentecost Myeloma Research Center (PMRC) multiple myeloma (MM) cohort consisting of newly diagnosed multiple myeloma (NDMM; 0 prior lines of therapy), early relapse multiple myeloma, (ERMM, 1-3 lines of prior therapy) and late relapse multiple myeloma (LRMM, >3 lines of prior therapy) patients. The expression of 30 sphingolipid metabolism genes was assessed in NDMM (N=187), ERMM (N=303) and LRMM (N=182). Each dot represents the median score for a gene.

b. Myeloma patients were divided into groups based on the average expression of 30 sphingolipid genes ($Sphingo^{Low}$ and $Sphingo^{High}$). Kaplan-Meier plots show the overall survival of ERMM and LRMM patients in $Sphingo^{Low}$ (average Z-score <0, n=234) and $Sphingo^{High}$ clusters (average Z-score >0 n=247). Inset indicates median survival in days.

c. The expression of ASAH1 mRNA was assessed in the PMRC MM cohort. The Violin plot shows the median expression of ASAH1 mRNA in NDMM (N=187), ERMM (N=303) and LRMM (N=182) patient samples. Dots represent individual patients.

d. The expression of ASAH1 mRNA was assessed in the PMRC MM cohort and patients were divided into NDMM and RRMM groups. The RRMM group was further subdivided based on the treatment regimen that each patient was given prior to relapse. The bubble blot shows the median ASAH1 expression (z-score) in newly diagnosed, or myeloma patients resistant to each indicated treatment. Colored bubbles represent median z–score of each group. Bubble size represents statistical

significance between newly diagnosed multiple myeloma and resistance to treatment.

e. Whole cell lysates were prepared from isogeneic PI-sensitive (U266, ANBL-6, 8226, 5TGM1) and PI-resistant (PSR, V10-R, B25, C40R, C100R, C300R) multiple myeloma cell lines. The immunoblot shows the expression of ASAH1 and the loading control, actin in each cell line.

f. The level of ceramide was assessed by flow cytometry in multiple myeloma cell lines, U266 and their PI-resistant derivative. The bar chart indicates the quantified median fluorescence intensity (MFI) of ceramide in each cell line (left). The level of sphingosine-1 phosphate (S1-P) was assessed by enzyme-linked immunosorbent assay (ELISA) in MM cell lines, U266 and their PI-resistant derivative, PSR. The bar chart shows the amount of intracellular S1-P in each cell line normalized to 100µg of total protein. (right). Values are mean ± SD of three independent experiments.

Statistical significance was derived by Ordinary one-way ANOVA with Dunnett's multiple comparisons test (**a**, **c** and **d**), Log-rank (Mantel-Cox) test (**b**) and Student's t test (**f**). p values of <0.05, <0.01, <0.001 and <0.0001 are represented by *, **, *** and **** respectively.

Figure 2. Inhibition of ASAH1 reduces proteasome inhibitor-resistant multiple myeloma cell growth *in vitro* and reduces tumor growth *in vivo*.

a. ASAH1 was knocked down by short hairpin RNA (shRNA) using two independent constructs in PSR MM. Control (CTRL) or ASAH1 knockdown (KD1/3) PSR cells were plated in 96-well plates ($0.3x10^6$ cells/ml) and allowed to grow proliferate. Cell viability was assessed by MTS at indicated time points. Values are mean ± SD of three independent experiments

b. A panel of commercial ASAH1 inhibitors were tested on ASAH1 activity (3 hours) and viability (72 hours) in PSR using the ASAH1 activity probe RBM14-C12 and MTS viability assay respectively. NR = IC_{50} not reached.

c. Sensitive (U266, 8226, ANBL-6, 5TGM1, MM1.S and OPM2) and drug-resistant MM (PSR, B25, V10-R, C100R, C300R, DOX6) were plated in 100µL in 96-well plates ($0.3x10^6$ cells/ml) with increasing concentrations of ceranib-2. Viability was assessed by MTS assay at 72hours, normalized to vehicle treated controls for each cell line. Box and whisker plots show the calculated IC_{50} values. Each dot represents the average IC_{50} of each cell line. Values are mean ± SD of three independent experiments

d. NOD.Cg-Prkdc scid Il2rg tm1Wjl /SzJ (NSG) mice were inoculated with PSR-RFP MM cells ($5x10^6$ cells/100µL) via the tail vein. Tumors were allowed to establish and proliferate for 21 days. Mice were randomized into three groups and treated with ceranib-2 (Cera-2, 5mg/kg/5 x week, n=8), bortezomib (BTZ, 0.5mg/kg/2 x week, 72 hours apart, n=9), or vehicle (n=7) until the end of study. The line graph shows the total radiant efficiency of mice (as a marker of tumor growth) in mice treated with

Cera-2 (n=8), BTZ (n=9), or vehicle (n=7) over the course of study and prior to mice reaching endpoint (hindlimb paralysis or >20% body weight lost) as measured by IVIS Lumina.

e. The bar chart indicates the total radiant efficiency of mice in Cera-2 (n=8), BTZ (n=9), or vehicle (n=7) treatment groups at the final time point in study that included all mice (day 63, left). Representative fluorescence images of red fluorescent protein positive (RFP+) MM in mice at day 63 (right).

f. The Kaplan-Meier plot shows the percentage of mice treated with Cera-2 (n=8), BTZ (n=9), or vehicle (n=7) reaching end point (hindlimb paralysis or >20% body weight lost) over the course of study.

Statistical significance was derived by ordinary one-way ANOVA with Dunnett's multiple comparisons test (**a** and **e**), Student's t test (**c**), two-way ANOVA with Šídák's correction (**d**) and Log-rank (Mantel-Cox) test (**f**). p values of <0.05, <0.01, <0.001 and <0.0001 are represented by *, **, *** and **** respectively.

Figure 3. Inhibition of ASAH1 increases ceramide production and reduces S1-P levels, and MCL-1 and BCL-2 phosphorylation and expression in proteasome inhibitor-resistant multiple myeloma.

a. Multiple myeloma (MM) patients from the Multiple Myeloma Research Foundation (MMRF) CoMMpass trial were divided into $ASAH1^{Low}$ (N=385) and $ASAH1^{High}$ (N=385) groups (median split). GSEA enrichment was performed on these patients' samples ($ASAH1^{High}$ - $ASAH1^{Low}$) to determine gene sets that were enriched in patients with elevated ASAH1. The bar chart shows the enriched gene sets in $ASAH1^{High}$ MM patients from the MMRF CoMMpass trial.

b. MM patients from the MMRF CoMMpass trial were divided into $ASAH1^{Low}$ (N=385) and $ASAH1^{High}$ (N=385) groups (median split). The expression of MCL-1 and BCL-2 in each group was assessed. The dot plots show the MCL-1 and BCL-2 gene expression in $ASAH1^{Low}$ (gray, n=385) $ASAH1^{High}$ (pink, n=385) CoMMpass patients. Each dot represents a patient sample

c. Whole cell lysates were prepared from PI-sensitive (U266) and PI-resistant (PSR) MM cells. The representative immunoblot shows the expression of ASAH1, pMCL-1 (T163), total MCL-1, p-BCL-2 (S70), total BCL-2 expression and the loading control actin. Numbers denote the molecular weight (kDa) of each protein.

d. Whole cell lysates were prepared from control or ASAH1 shRNA knockdown (KD1-3) PI-resistant PSR MM cells (left) or PSR cells treated with 2 μM ceranib-2 for indicated number of hours (right). The representative immunoblot shows the

expression of ASAH1, pMCL-1 (T163), total MCL-1, p-BCL-2 (S70), total BCL-2 expression and the loading control actin.

e. Bar charts showing the median fluorescence intensity (MFI) of ceramide levels (top) and sphingosine-1 phosphate (S1P) levels (bottom) in control (CTRL) or ASAH1 knockdown (KD1/3) PSR cells and PSR cells treated with vehicle or ceranib-2 (2μM) for 24 hours as assessed by flow cytometry and enzyme-linked immunosorbent assay (ELISA) respectively. Values are mean ± SD of three independent experiments.

f. Whole cell lysates were prepared from PSR MM cells treated with indicated concentrations of the sphingosine kinase inhibitor, SKI-178 or ceramide C6 for 4 hours The representative immunoblot show the expression of total MCL-1, total BCL-2 expression and the loading controls actin or vinculin. Numbers denote the molecular weight (kDa) of each protein.

Statistical significance was derived by unpaired t test (**b** and **e** top right panel) and ordinary one-way ANOVA with Dunnett's multiple comparisons test (**e** top left and bottom panels). p values of <0.05, <0.01, <0.001 and <0.0001 are represented by *, **, *** and **** respectively

Figure 4. Inhibition of ASAH1 restores PI sensitivity in proteasome inhibitor-resistant multiple myeloma cells *in vitro* and *in vivo* through loss of antiapoptotic proteins.

a. U266, CTRL (PSR) and ASAH1 KD (PSR KD1/3) MM cells were plated in 100μL in 96-well plates ($0.3x10^6$ cells/ml) with the indicated concentrations of the proteasome

inhibitor, bortezomib (BTZ). Cell viability was assessed at 24 hours by the MTS assay. The bar chart shows the effect of BTZ on U266, CTRL (PSR) and ASAH1 KD (KD1/3) PSR cell viability. Values are mean ± SD of three independent experiments.

b. PI resistant PSR MM cells were plated in 100µL in 96-well plates ($0.3x10^6$ cells/ml) with either vehicle, ceranib-2, carfilzomib or a combination of both drugs at the indicated concentrations for 72-hours. Viability was assessed by MTS assay, normalized to the vehicle treated control and LOEWE synergy was calculated using Combenefit. The representative LOEWE synergy plot shows the depth of response (xyz) and the level of antagonism/synergy of ceranib-2 and carfilzomib combinations. Blue areas indicated synergy.

c. Diagram of *in vivo* study to assess the ASAH1 knockdown on PSR-RFP cell growth. CTRL or ASAH1 knockdown (KD) PSR-RFP cells were injected i.v. IgE was detected 3-weeks post inoculation. Mice were subdivided into groups and treated with vehicle (Veh), or bortezomib (BTZ; 0.5 mg/kg, twice weekly M/Th). All mice were sacrificed when first mouse reached end-point criteria.

d. Serum was isolated by submandibular bleed and the levels of paraprotein (IgE) were assessed by ELISA in CTRL-vehicle (n=9), ASAH1KD-vehicle (n=10) CTRL-BTZ (n=10), ASAH1KD-BTZ (n=9) mice over course of study.

e. At the study endpoint (the time at which the first mouse developed hindlimb paralysis) all mice were sacrificed and bone marrow cells from the left tibia and femur pair were isolated and subject to flow cytometry. The bar chart shows the percentage of HLA-A/B/C positive cells (as a marker of human MM cells) in the bone

marrow of CTRL-vehicle (n=9), ASAH1KD-vehicle (n=10) CTRL-BTZ (n=10), ASAH1KD-BTZ (n=9) mice at study endpoint.

f. At the study endpoint (the time at which the first mouse developed hindlimb paralysis) all mice were sacrificed and bone marrow cells from the left tibia and femur pair were isolated and subject to flow cytometry. The bar chart shows the percentage of MCL-1 positive (left) and BCL-2 positive (right) HLA-A/B/C positive (MM) cells in the bone marrow of CTRL-vehicle (n=9), ASAH1KD-vehicle (n=10) CTRL-BTZ (n=10), ASAH1KD-BTZ (n=9).

Statistical significance was derived by ordinary one-way ANOVA with Dunnett's multiple comparisons test (**d-f**). p values of <0.05, <0.01, and <0.001 are represented by *, **, and *** respectively.

Figure 5. ASAH1 inhibition activates PP2A through ceramide-mediated SET inhibition.

a. Whole cell lysates from control and ASAH1 KD PI-resistant (PSR and B25) multiple myeloma (MM) cells were subject to pSTY phosphoproteomic analysis. Significantly upregulated and down regulated pSTY sites were underwent ROKAI (Robust inference of kinase activity) analysis to infer changes in phosphatase activity. The bar chart shows the changes in inferred phosphatase activities following ASAH1 knockdown in PI-resistant MM cells (PSR and B25).

b. PP2A activity was assessed in PSR cells following ASAH1 knockdown, or control cells treated with vehicle, ceranib-2 (5 µM) or C6 ceramide (50 µM) for 4 hours, with or without PP2A-specific inhibitor (Okadaic acid, 1 nM). Values are mean ± SD of four independent experiments.

c. Whole cell lysates were prepared from PSR cells transfected with non-targeting siRNA (NTsi) or SET-targeting siRNA (SETsi) 48 hours post transfection. The representative immunoblot shows SET isoforms 1 and 2, total and phosphorylated MCL-1, BCL-2 and the loading control actin 48 hours post transfection.

d. Pi-resistant PSR cells were transfected with non-targeting siRNA (NTsi) or SET-targeting siRNA (SETsi). After 48 hours, cells were plated in 100µL in 96-well plates ($0.3x10^6$ cells/ml) with indicated concentrations of bortezomib. After 24 hours (72 hours post transfection) MM cell viability was assessed by MTS assay and viability was normalized to vehicle treated NTsi PSR cells. The bar chart shows the effect of SETsi alone and in combination with the proteasome inhibitor, BTZ. Values are mean ± SD of three independent experiments.

e. The median expression of SET, ASAH1, MCL-1 and BCL-2 in NDMM, ERMM and LRMM patients from the PMRC RNA-seq dataset was assessed. Each dot represents the median expression of a gene in each patient group. NDMM, ERMM and LRMM contain 187, 303 and 182 patients respectively.

f. Schematic diagram of PI-resistant MM cells under normal conditions (left) and following ASAH1 inhibition (right). Following ASAH1 inhibition, ceramide levels accumulate and reduce the pool of sphingosine-1 phosphate (S1-P). Ceramide binds to and inhibits SET, thus activating the phosphatase PP2A. PP2A targets BCL-2 and MCL-1 reducing their activity and expression. Reduced levels of anti-apoptotic proteins reduce PI-resistant cell viability and render them sensitive to proteasome inhibition and apoptosis.

Statistical significance was derived by ordinary one-way ANOVA with Dunnett's multiple comparisons test (**b, d, e**). p values of <0.05, <0.01, <0.001 and <0.0001 are represented by *, **, *** and **** respectively.

Figure 6. Ceranib-2 synergizes with carfilzomib in most *ex vivo* multiple myeloma patient samples.

a. Schematic diagram of *ex vivo* mathematical myeloma advisor (EMMA) platform. CD138+ multiple myeloma (MM) cells and bone marrow stroma are isolated from patients and cultured in 384-well plates with drugs for 6 days. Five concentrations of each drug are used. Live cell imaging is used to assess viability over time and median area under the curve (AUC) per patient is calculated at 96 hours.

b. Newly diagnosed multiple myeloma (NDMM, n=22) and relapsed/refractory multiple myeloma (RRMM, n=32) patients' cells were exposed to 5 concentrations of ceranib-2 in the EMMA platform. The box and whisker plot demonstrates the median AUC for patient groups. Each dot represents a different patient.

c. The AUC for different drugs were normalized to the median AUC of each drug. The box plot shows the normalized AUCs of indicated drugs in newly diagnosed multiple myeloma (NDMM) and relapsed/refractory multiple myeloma (RRMM) patients and only ceranib-2 (Cera-2) is significantly more effective in relapsed/refractory multiple myeloma (RRMM) patients. Arrows indicate differences in the newly diagnosed multiple myeloma (NDMM) and relapsed/refractory multiple myeloma (RRMM) patient.

d. Thirty patients with plasma cell malignancies (1 smoldering MM (SMOL), 1 plasma cell leukemia (PCL), 14 NDMM, and 14 RRMM patients) were exposed to ceranib-2, carfilzomib or a combination of both drugs in the EMMA platform. The box and whisker plot shows the median AUC of the 30 patients' response *ex vivo* to single

agent ceranib-2 (cera-2), carfilzomib (CFZ), or the combination – either additive or observed. Additive represents the expected value of combining two agents whereas observed indicates the actual response. The difference between additive and observed values is used to calculate either synergy or antagonism. Red dots and lines represent synergy whereas blue lines and dots represents antagonism.

e. The level of synergy or antagonism was assessed in 30 patients treated ceranib-2 and carfilzomib. The bar chart shows level of synergy or antagonism (the difference between additive and observed combinations) seen when ceranib-2 and carfilzomib were combined to treat 1 smoldering multiple myeloma (SMOL), 1 plasma cell leukemia (PCL), 14 newly diagnosed multiple myeloma, and 14 relapsed/refractory multiple myeloma patients *ex vivo*. Positive values indicate synergy whereas negative values indicate antagonism.

f. Box and whisker plot indicating the level of synergy/antagonism in carfilzomib-sensitive (1^{st} quartile, n=7), carfilzomib-responsive (2^{nd} and 3^{rd} quartiles, n=17) and carfilzomib-resistant (4^{th} quartile, n=4) multiple myeloma patients. Quartiles were identified based on the area under the curve of carfilzomib responses of 619 multiple myeloma patients previously tested *ex vivo*

Statistical significance was derived by unpaired t test (**b**), ordinary one-way ANOVA with Šídák's correction (**c**), with Dunnet's correction (**d** and **f**). p values of <0.05 are represented by *.

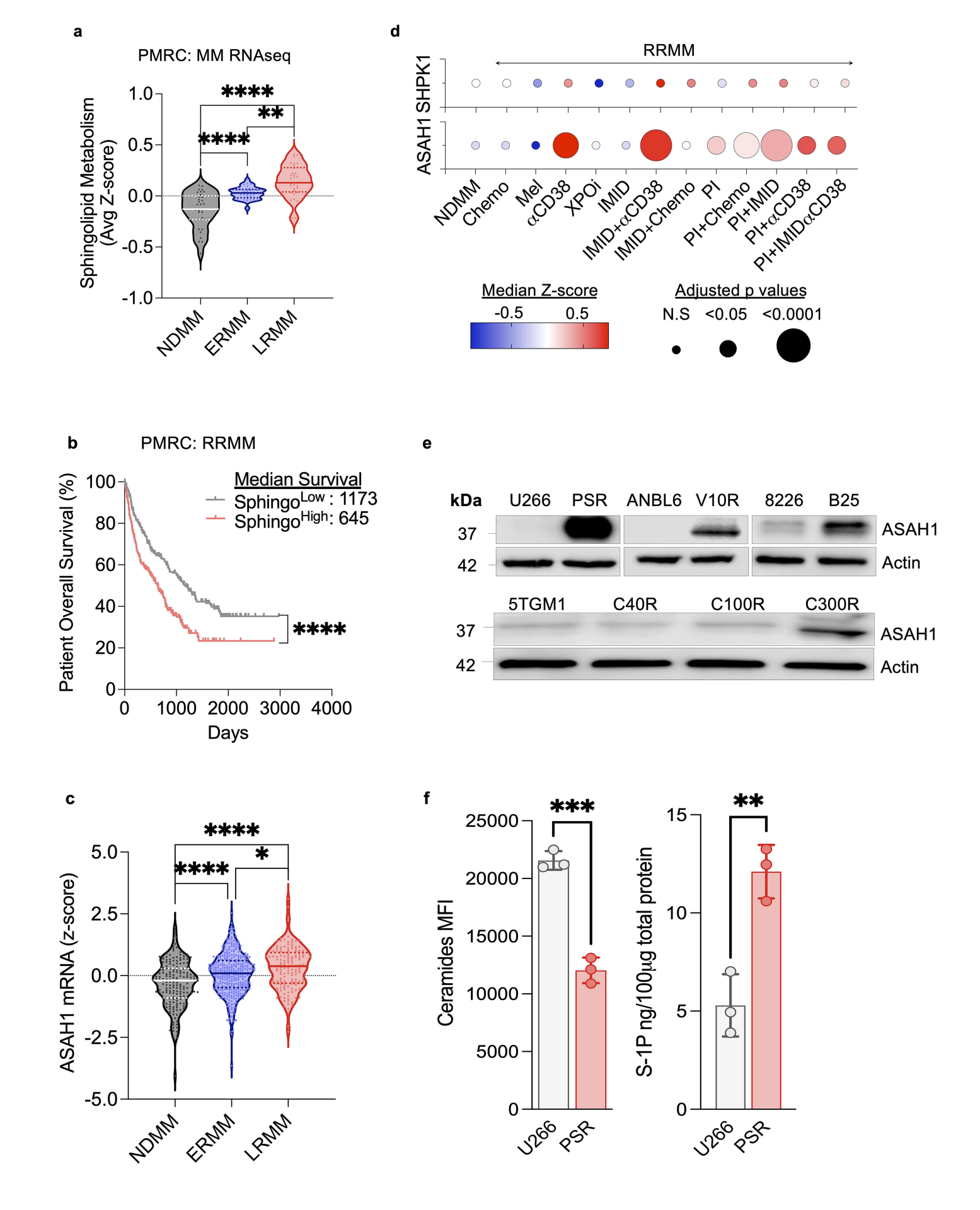
a
PMRC: MM RNAseq
Sphingolipid Metabolism (Avg Z-score)
1.0
0.5
0.0
-0.5
-1.0
****
**
****
NDMM
ERMM
LRMM
d
RRMM
ASAH1
SHPK1
NDMM
Chemo
Mel
αCD38
XPOi
IMID
IMID+αCD38
IMID+Chemo
PI
PI+Chemo
PI+IMID
PI+αCD38
PI+IMIDαCD38
Median Z-score
-0.5
0.5
Adjusted p values
N.S
<0.05
<0.0001
b
PMRC: RRMM
Patient Overall Survival (%)
100
80
60
40
20
0
Median Survival
Sphingo^Low : 1173
Sphingo^High: 645
****
0
1000
2000
3000
4000
Days
e
kDa
U266
PSR
ANBL6
V10R
8226
B25
37
42
ASAH1
Actin
5TGM1
C40R
C100R
C300R
37
42
ASAH1
Actin
c
ASAH1 mRNA (z-score)
5.0
2.5
0.0
-2.5
-5.0
****
****
*
NDMM
ERMM
LRMM
f
Ceramides MFI
25000
20000
15000
10000
5000
0
***
U266
PSR
S-1P ng/100µg total protein
15
10
5
0
**
U266
PSR

a

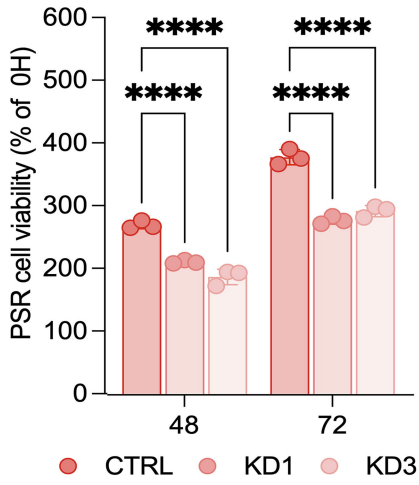

b

Inhibitor	ASAH1 IC_{50} (μM)	PSR IC_{50} (μM)
Ceranib-2	2.146	0.89
LCL-521	5.130	0.75
Carmofur	19.61	13.01
ARN-14998	NR	86.37
ARN-14974	NR	346.1

c

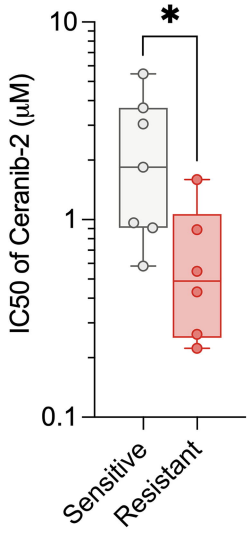

d

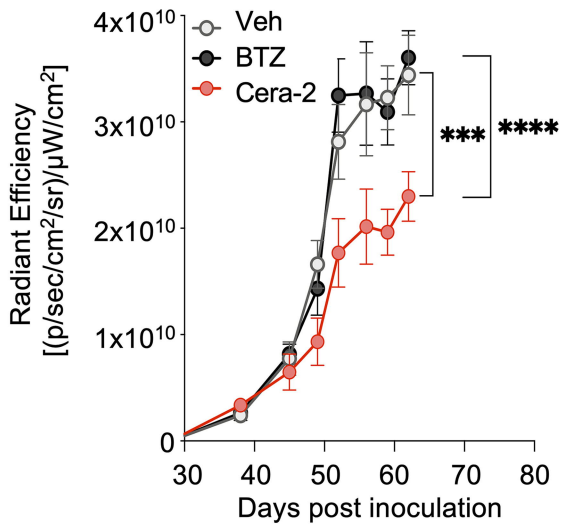

e

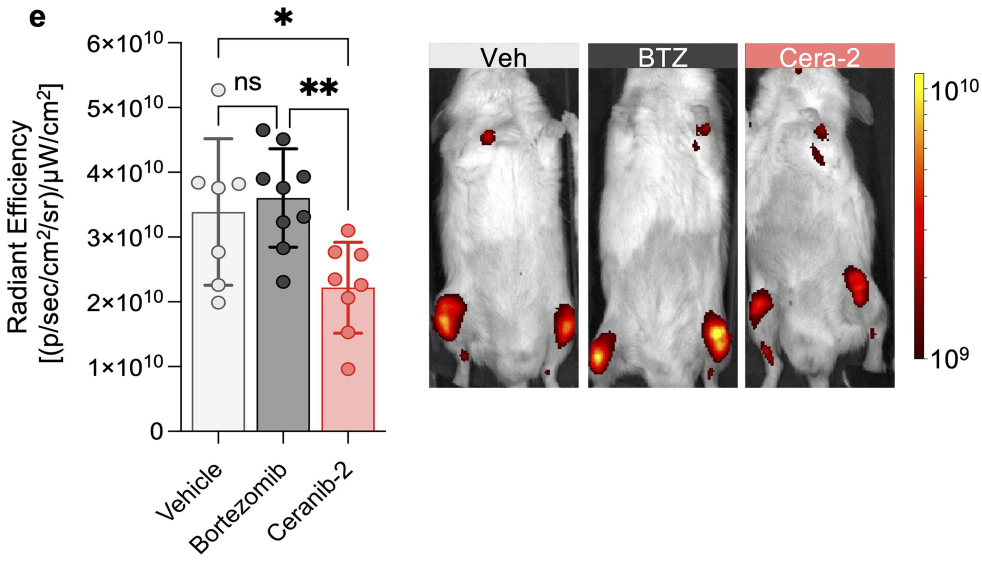

f

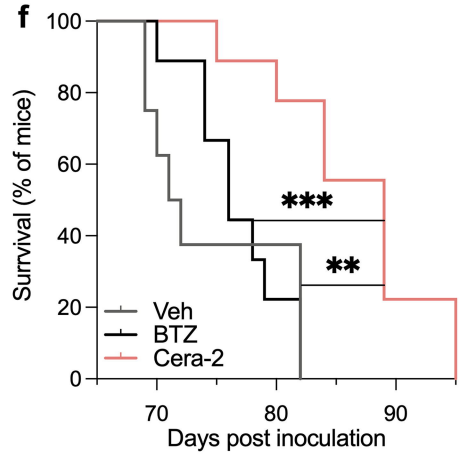

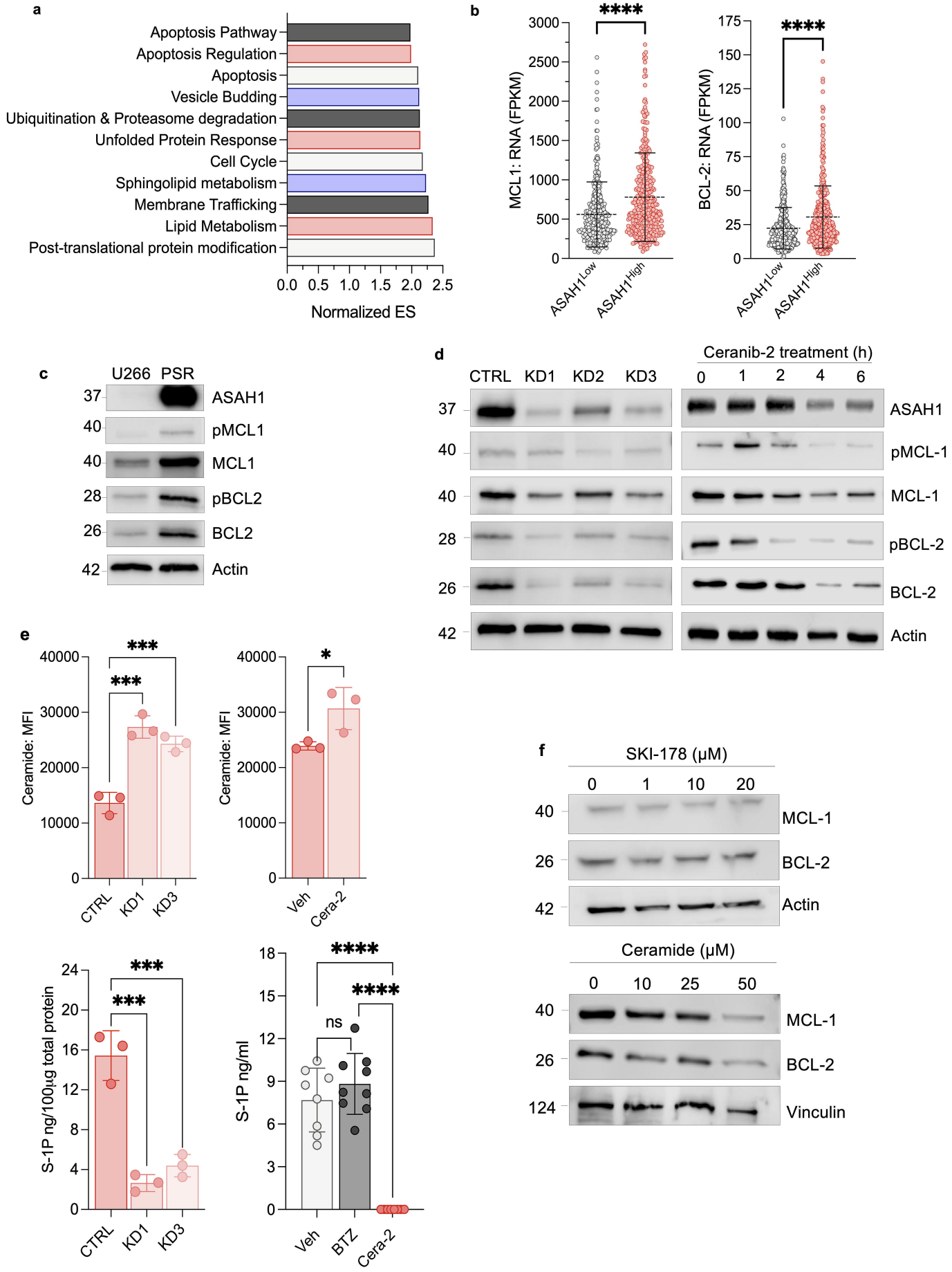
a
Apoptosis Pathway
Apoptosis Regulation
Apoptosis
Vesicle Budding
Ubiquitination & Proteasome degradation
Unfolded Protein Response
Cell Cycle
Sphingolipid metabolism
Membrane Trafficking
Lipid Metabolism
Post-translational protein modification
0.0 0.5 1.0 1.5 2.0 2.5
Normalized ES
b
****
MCL1: RNA (FPKM)
3000
2500
2000
1500
1000
500
0
ASAH1Low
ASAH1High
****
BCL-2: RNA (FPKM)
175
150
125
100
75
50
25
0
ASAH1Low
ASAH1High
c
U266 PSR
37 ASAH1
40 pMCL1
40 MCL1
28 pBCL2
26 BCL2
42 Actin
d
Ceranib-2 treatment (h)
CTRL KD1 KD2 KD3
0 1 2 4 6
37 ASAH1
40 pMCL-1
40 MCL-1
28 pBCL-2
26 BCL-2
42 Actin
e
***
***
Ceramide: MFI
40000
30000
20000
10000
0
CTRL KD1 KD3
*
Ceramide: MFI
40000
30000
20000
10000
0
Veh Cera-2
***
***
S-1P ng/100µg total protein
24
20
16
12
8
4
0
CTRL KD1 KD3
****
****
ns
S-1P ng/ml
18
15
12
9
6
3
0
Veh BTZ Cera-2
f
SKI-178 (µM)
0 1 10 20
40 MCL-1
26 BCL-2
42 Actin
Ceramide (µM)
0 10 25 50
40 MCL-1
26 BCL-2
124 Vinculin

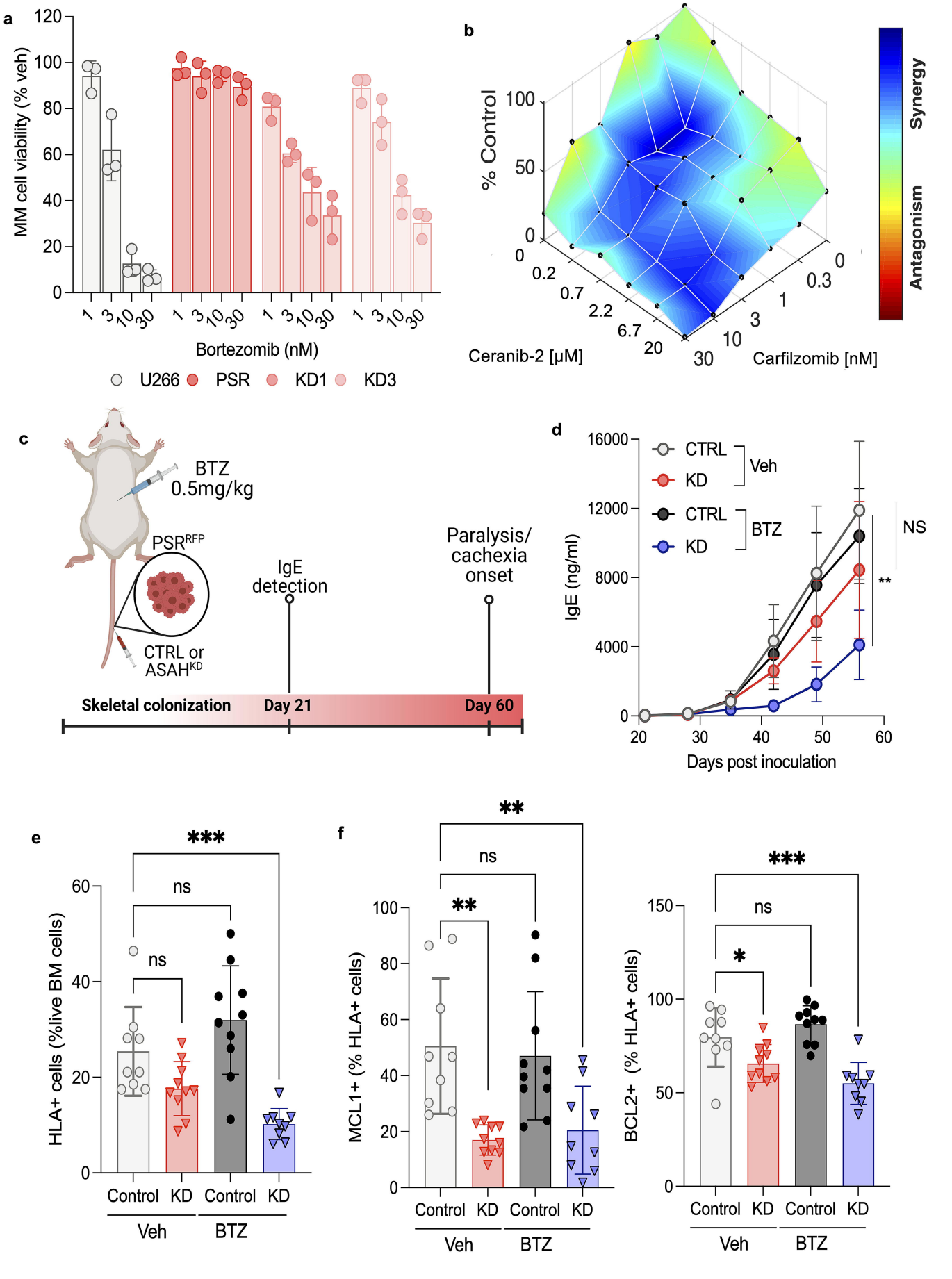
a
MM cell viability (% veh)
Bortezomib (nM)
U266
PSR
KD1
KD3
b
% Control
Ceranib-2 [μM]
Carfilzomib [nM]
Synergy
Antagonism
c
BTZ
0.5mg/kg
PSRRFP
CTRL or
ASAHKD
IgE
detection
Paralysis/
cachexia
onset
Skeletal colonization
Day 21
Day 60
d
IgE (ng/ml)
CTRL
KD
Veh
BTZ
NS
Days post inoculation
e
HLA+ cells (%live BM cells)
Control
KD
Veh
BTZ
f
MCL1+ (% HLA+ cells)
BCL2+ (% HLA+ cells)
ns

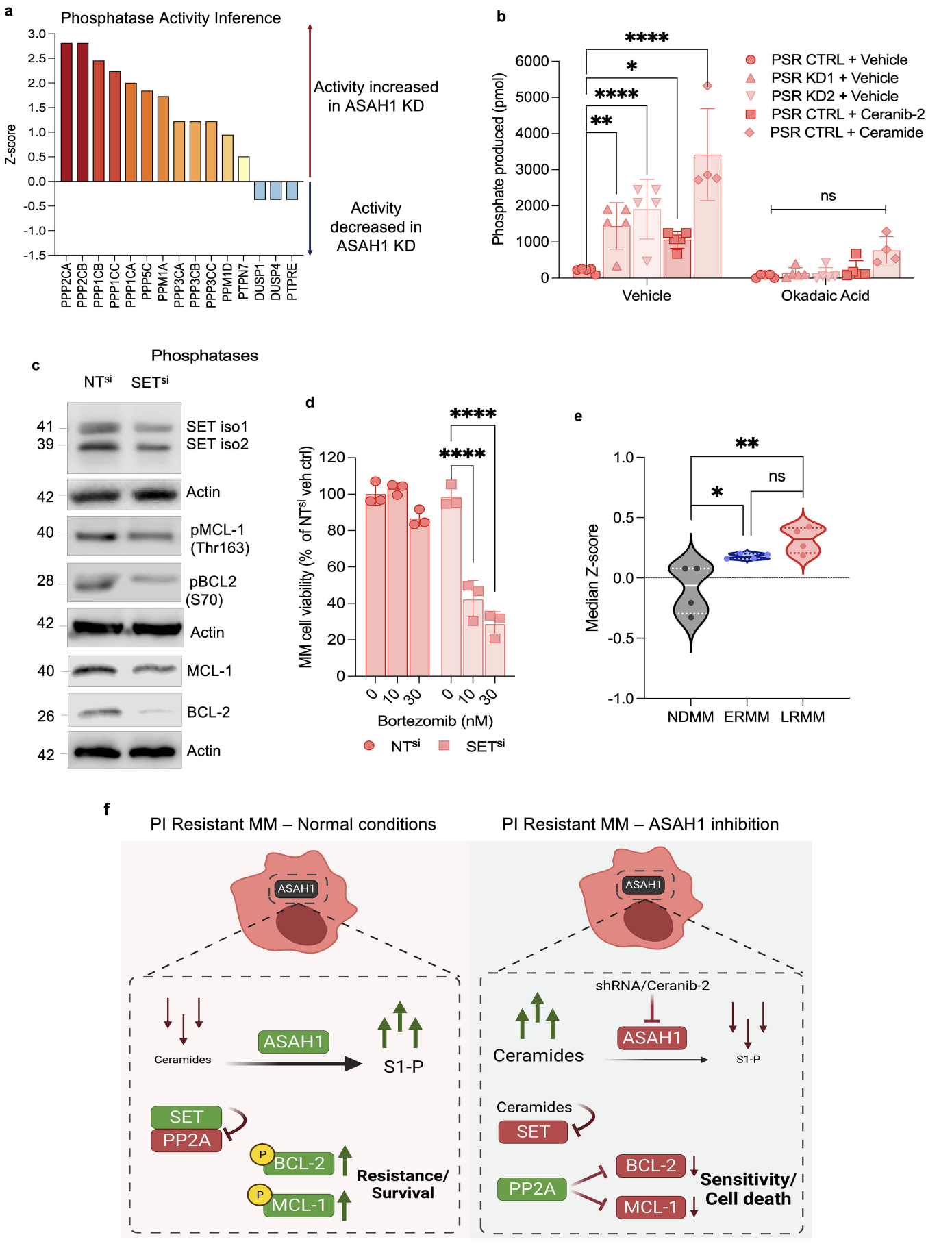
a
Phosphatase Activity Inference
Z-score
Activity increased in ASAH1 KD
Activity decreased in ASAH1 KD
PPP2CA
PPP2CB
PPP1CB
PPP1CC
PPP1CA
PPP5C
PPM1A
PPP3CA
PPP3CB
PPP3CC
PPM1D
PTPN7
DUSP1
DUSP4
PTPRE
b
Phosphate produced (pmol)
PSR CTRL + Vehicle
PSR KD1 + Vehicle
PSR KD2 + Vehicle
PSR CTRL + Ceranib-2
PSR CTRL + Ceramide
ns
Vehicle
Okadaic Acid
c
Phosphatases
NTsi
SETsi
SET iso1
SET iso2
Actin
pMCL-1 (Thr163)
pBCL2 (S70)
Actin
MCL-1
BCL-2
Actin
d
MM cell viability (% of NTsi veh ctrl)
Bortezomib (nM)
NTsi
SETsi
e
Median Z-score
NDMM
ERMM
LRMM
f
PI Resistant MM – Normal conditions
PI Resistant MM – ASAH1 inhibition
ASAH1
Ceramides
S1-P
SET
PP2A
BCL-2
MCL-1
Resistance/ Survival
shRNA/Ceranib-2
Sensitivity/ Cell death

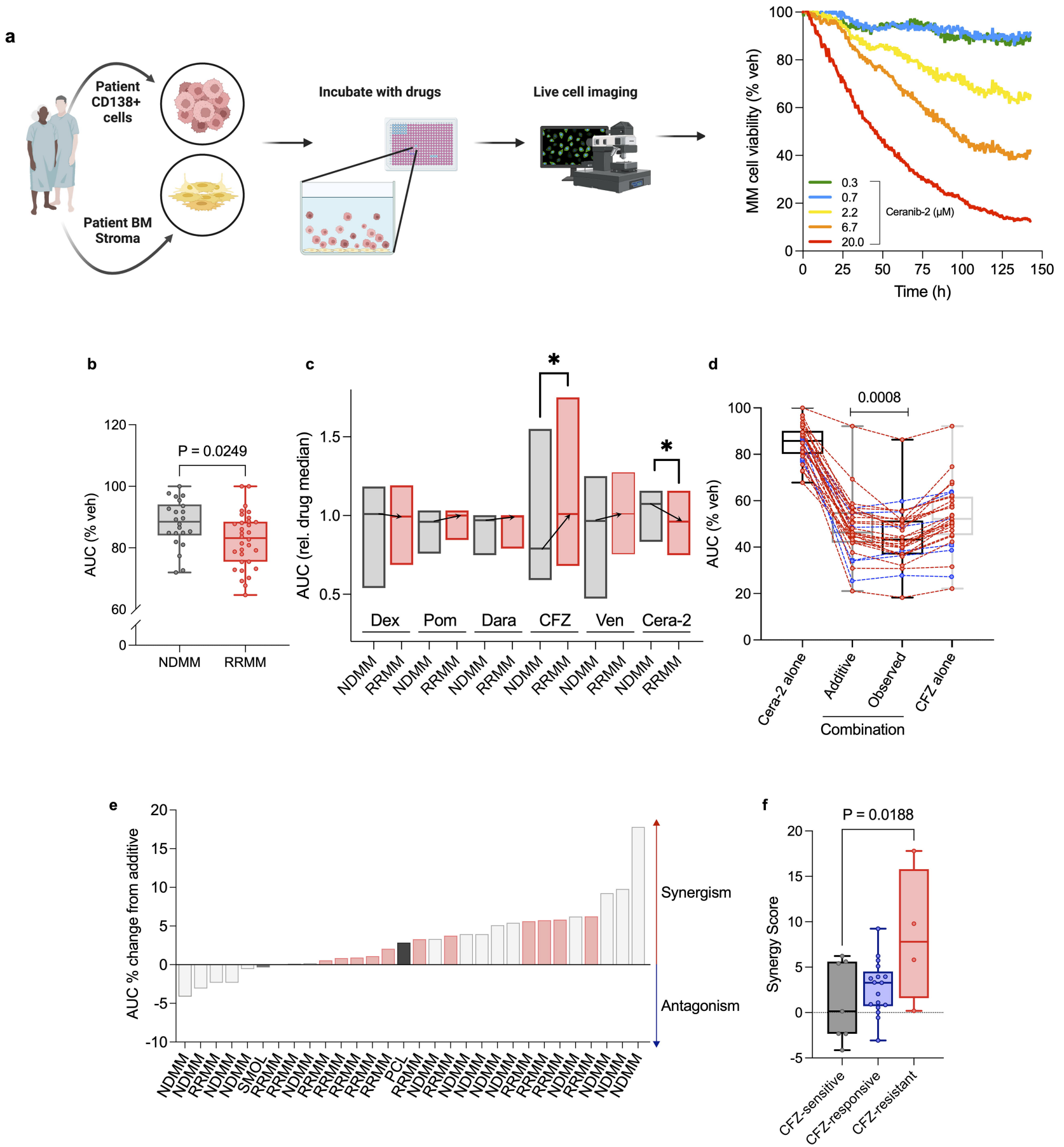
a
Patient CD138+ cells
Patient BM Stroma
Incubate with drugs
Live cell imaging
MM cell viability (% veh)
Time (h)
0.3
0.7
2.2
6.7
20.0
Ceranib-2 (μM)
b
AUC (% veh)
P = 0.0249
NDMM
RRMM
c
AUC (rel. drug median)
Dex
Pom
Dara
CFZ
Ven
Cera-2
d
AUC (% veh)
0.0008
Cera-2 alone
Additive
Observed
CFZ alone
Combination
e
AUC % change from additive
Synergism
Antagonism
f
Synergy Score
P = 0.0188
CFZ-sensitive
CFZ-responsive
CFZ-resistant

Supplementary Materials and Methods:

Sample Preparation and RNA Sequencing Analysis: PMRC Cohort

Fresh BM aspirate cells were enriched for CD138 expression using Miltenyi (Bergisch Gladbach, Germany) 130-051-301 antibody-conjugated magnetic beads. 1.0 x 10^6 viably frozen CD138+ cells were shipped for molecular analysis in the context of the ORIEN Avatar program.

Nucleic Acid Extraction: For frozen tissue DNA extraction, Qiagen QIASymphony DNA purification was performed, generating 213 bp average insert size. For frozen tissue RNA extraction, Qiagen RNAeasy plus mini kit was performed, generating 216 bp average insert size.

RNA Sequencing was performed using the Illumina TruSeq RNA Exome with single library hybridization, cDNA synthesis, library preparation, sequencing (at either 100 or 150 bp paired reads) to a coverage of 100M total reads / 50M paired reads.

RNA-seq Tumor Pipeline Analysis is processed according to the workflow outlined below using GRCh38/hg38 human genome reference sequencing and GenCode build version 32.

Adapter trimming: Adapter sequences are trimmed from the raw tumor sequencing FASTQ file. Adapter-trimming via *k*-mer matching is performed along with quality-trimming and filtering, contaminant-filtering, sequence masking, GC-filtering, length filtering and entropy-filtering. The trimmed FASTQ file is used as input to the read alignment process.

Read Alignment: The tumor adapter-trimmed FASTQ file is aligned to the human genome reference (GRCh38/hg38) and the Gencode genome annotation v32 using the STAR aligner. The STAR aligner generates multiple output files used for Gene Fusion Prediction and Gene Expression Analysis.

RNA expression: RNA expression values are calculated and reported using estimated mapped reads, Fragments Per Kilobase of transcript per Million mapped reads (FPKM), and Transcripts Per Million mapped reads (TPM) at both transcript level and gene level based on transcriptome alignment generated by STAR. Gene expression data was obtained from DNAnexus files containing FPKM and TPM values for 59,368 records. Among these, 19,933 were protein coding genes, which were further analyzed; the remainder were discarded. For each gene/sample, we have calculated $\log2(FPKM+10^{-3})$ and removed any genes whose values for quartile 1 and quartile 3 were the same (i.e., any gene must be expressed in at least 25% of samples to be considered in this analysis). The remaining 16,738 genes were Z-normalized across all samples using MATLAB's function *normalize*.

Cell lines, culture conditions and compounds

Supplementary Figures and Legends

Luciferase-labeled MM cells, 5TGM1-Luc (RRID: CVCL_VI66) and U266-Luc (RRID: CVCL_0566) were obtained from University of Texas, Health Science Center at San Antonio, TX (2012) and University of Virginia, VA (2014), respectively. MM1.S were obtained in 2015 from ATCC (RRID: CVCL_8792) and OPM2 was obtained in 2015 from Dr. Kenneth Shain (Moffitt Cancer Center; RRID: CVCL_1625). Isogenic PI-sensitive and resistant pairs U266 and PSR[1], RPMI8226 (RRID: CVCL_0014) and B25 [2], were obtained from Dr. Steven Grant (VCU-Massey) and ANBL-6 (RRID:CVCL_5425) and V10-R[3] pairs were obtained from Dr. Kenneth Shain (Moffitt Cancer Center). C300R, C100R and C40R (PI-resistant 5TGM1-Luc) cells were generated in house by continued culture in increasing concentration of carfilzomib for 3 months. C300R, C100R and C40R were exposed to 300nM, 100nM or 40nM maximum doses of carfilzomib, respectively. PI-resistant cell lines were maintained through bi-weekly 24-hour dosing with either bortezomib (30nM) or carfilzomib (300nM), cells were not used for five days following PI-treatment. All MM cell lines were maintained below $1x10^6$ cells/ml in RPMI-1640 containing 10% heat-inactivated FBS (PEAK, PK-FBS1), 1% penicillin and streptomycin and used within 20 passages. ANBL-6 and V10-R are IL-6 dependent cell lines, as such 1ng/ml IL-6 (R&D systems, HZ-1019) was added in cultures and all subsequent experiments. Human MSCs were obtained from Lonza (PT-2501) and cultured in αMEM (Gibco # 12561056) with 10% heat-inactivated qualified FBS (Gibco #26140079). Cells have recently tested negative for mycoplasma by PCR in December 2022 (Bulldog Bio, Cat #: 25233), and were additionally authenticated against ATCC, DSMZ or ExPASy STR profiles. The acid ceramidase inhibitors ceranib-2 (#11092), LCL-521 (#29738), carmofur (#14243) and ARN-14988 (#24284) and the proteasome inhibitors, bortezomib (#10008822) and carfilzomib (#17554) were purchased from Selleckchem. The acid ceramidase activity probe RBM14C12 (#860855), C6 ceramide (d18:1/6:0, # 860506) Huzzah-S1-P (#360492) and Huzzah-HSA (#360000) were purchased from Avanti polar lipids.

Lentiviral Transductions

Lentiviral particles with 4 individual shRNAs were generated following transformation of HEK-293 cells. MM cells were transduced with either ASAH1-targeting shRNA or non-targeting shRNA control lentivirus by spinfection with vectofusin-1 (Miltenyi Biotec # 130-111-163) at an MOI of 5. Cells were selected with puromycin (2μg/ml) for 72 hours. Knockdown was confirmed by immunoblotting. PSR-RFP were generated as above using lentiviral particles (Qiagen CLS-PCR-8) and FACS sorted.

Acid ceramidase activity assay

Supplementary Figures and Legends

To determine ceramidase activity in intact cells (5×10^4 cells/well) were seeded in 96-well plates in 100µl medium or PBS containing 40 µM RBM14C12 fluorogenic substrate incubated for 24 h at 37°C in a 5% CO2 atmosphere. To examine the effect of ceramidase inhibitors, cells were incubated with RBM14C12 for 3 hours. The reaction was stopped by addition of methanol followed by NaIO4 (2.5 mg/ml in 200 mM glycine/NaOH buffer, pH 10.6). After 1 h at 37°C, 100µl of 200 mM glycine/NaOH buffer were added, and fluorescence detected at 355/460nm excitation/emission wavelengths on a SpectraMax Microplate Reader (Molecular Devices, Sunnyvale, CA).

Immunoblotting

MM cells were lysed in RIPA buffer (150 mM NaCl, 1 mM EDTA, 1% Triton X-100, 1% sodium deoxycholate, 0.1% SDS, 20 mM Tris, pH 8). Protein concentration was determined by BCA (Pierce, Waltham, MA, USA; #23225). Blots were blocked in 5% BSA or TBS-T for 1 h followed by incubation with primary antibody overnight at 4°C. Primary antibodies were anti-ASAH1 (Thermofisher #HPA005468 or Pro-sci Inc #4741) , anti-actin (CST #3700), anti-BCL2 (CST #4223), anti-pBCL S70 (CST #2827), anti-MCL-1 (CST #94296), anti-p-MCL1 Thr163 (CST #14765), anti-vinculin (CST #13901) and diluted in blocking buffer. Blots were washed in TBS-T and incubated with either anti-rabbit IgG or anti-mouse IgG HRP-conjugated secondary antibodies (CST#7074 and #7076) and developed by enhanced chemiluminescence and imaging by LI-COR Odyssey Fc.

Viability and dose response assays

MM cell lines were plated in 96-well plates at a density of 2×105 cells/ml. Cells were treated with vehicle or indicated compounds. Cell viability was assessed at 24 or 72 hours by the MTT assay following the manufacturer's instructions (CellTiter 96, #G3582, Pierce.) The absorbance was measured at 490nm after 3 hours of incubation at 37°C. IC50s were calculated in Prism (version 9.3.1). Synergy matrices were calculated and generated using Combenefit.

***Ex vivo* drug sensitivity characterization: PMRC cohort**. An *ex vivo* assay was used to quantify the chemosensitivity of primary MM cells. Fresh BM aspirate cells were enriched for $CD138^+$ expression using Miltenyi (Bergisch Gladbach, Germany) 130-051-301 antibody-conjugated magnetic beads. MM cells ($CD138^+$) were seeded in Corning (Corning, NY) CellBIND 384 well plates with collagen I and previously established human-derived stroma, containing approximately 4000 MM cells and 1000 stromal cells. Each well was filled with 80 µL of Roswell

Supplementary Figures and Legends

Park Memorial Institute (RPMI) 1640 media supplemented with fetal bovine serum (FBS, heat inactivated), penicillin/streptomycin, and patient-derived plasma (10%, freshly obtained from patient's own aspirate, filtered) and left overnight for adhesion of stroma. The next day, drugs were added using a robotic plate handler so that every drug/combination was tested at 5 (fixed concentration ratio, for combinations) concentrations (1:3 serial dilution) in two replicates. Negative controls (supplemented growth media with and without the vehicle control dimethyl sulfoxide (DMSO)) were included, as well as positive controls for each drug (cell line MM1.S at highest drug concentration). Plates were placed in a motorized stage microscope (EVOS Auto FL, Life Technologies, Carlsbad, CA) equipped with an incubator and maintained at 5% CO_2 and 37 °C. Each well was imaged every 30 min for a total duration of up to 6 days. A digital image analysis algorithm[4] was implemented to determine changes in viability of each well longitudinally across the 96 or 144 hr intervals. This algorithm computes differences in sequential images and identifies live cells with continuous membrane deformations resulting from their interaction with the surrounding extracellular matrix. These interactions cease upon cell death. By applying this operation to all 288 images acquired for each well, we quantified non-destructively, and without the need to separate the stroma and MM, the effect of drugs as a function of concentration and exposure time. Digital image analysis computes percent viability of MM cells for each time point and experimental condition (drug and concentration). For each patient-drug, we have a dose-time-response surface, which is abstracted into AUC (area under the curve), which is an area/integral measure of *ex vivo* response to therapy computed by taking an average of all *ex vivo* responses across all time (first 96h) and concentration.

Flow cytometry

For *ex vivo* analysis, tibia and femur were used to assess tumor burden by RFP or HLA-A/B/C expression. Tibial ends were excised, whole bone marrow was isolated by centrifugation at 10,000g for 10 seconds. Red blood cells were lysed by RBC lysis buffer (R7757, Sigma-Aldrich) as per manufacturers guidelines. Bone marrow cells were subject to viability staining with Zombie Near-Infrared (NIR; 1:500; 423105, BioLegend). Appropriate compensation and fluorescence-minus-one (FMO) controls were generated in parallel either with aliquots of bone marrow cells or PSR RFP+/-. Stained controls and samples were analyzed using BD Biosciences LSRII flow cytometer. The percentage of RFP+ or HLA-expressing cells was gated on singlet live bone marrow cells. The presence of BCL-2 and MCL-1 was assessed in HLA-expressing cells. FCS Express 7 was used to perform gating post acquisition.

Supplementary Figures and Legends

Microcomputed Tomography.

Harvested tibiae were fixed in 4% PFA for 48 hours. Tibiae from mice from all time points were centralized and were subjected to micro-computed topography (μCT) scanning using Scanco μ35 scanner to elucidate bone volume data at the proximal tibial metaphases. Individual bone scans were deidentified using numerical codes during, and reidentified post analyses in a blinded fashion. Evaluation of trabecular bone microarchitecture was performed in a region that consisting of 1000 μm, beginning 120 μm from the growth plate. A three-dimensional cubical voxel model of bone was built and calculations were made for relative bone volume per total volume (BV/TV), trabecular number (Tb.N), trabecular thickness (Tb.Th), trabecular spacing (Tb.Sp) and connectivity density (Conn.D).

Phosphoproteomics

PI-resistant PSR or B25 cells that were transduced with control or ASAH1-targeting shRNA (ASAH1 KD) were subject to phosphoproteomic analysis. Cells were lysed in denaturing buffer containing 8 M urea, 20 mM HEPES (pH 8), 1 mM sodium orthovanadate, 2.5 mM sodium pyrophosphate and 1 mM β-glycerophosphate. Bradford assays determined the protein concentration for each sample. Aliquots of 200 μg were prepared for global phosphorylation. Protein disulfides were reduced with 4.5 mM DTT at 60 °C for 30 minutes and then cysteines were alkylated with 10 mM iodoacetamide for 20 minutes in the dark at room temperature. Trypsin digestion was carried out at room temperature overnight with enzyme to substrate ratio of 1:20, and tryptic peptides were acidified with aqueous 1% trifluoroacetic acid (TFA) and desalted with C18 Sep-Pak cartridges according to the manufacturer's procedure. For global phosphorylation, 200 μg of each tryptic digest was TMT labeled. Label incorporation was verified to be >95% by LC-MS/MS and spectral counting. The samples were then pooled and lyophilized. The TMT channel layouts were:

126C PSR control Rep1; 127N PSR KD Rep1; 127C PSR control Rep2; 128N PSR KD Rep2; 128C PSR control Rep3; 129N PSR KD Rep3; 129C PSR control Rep4; 130N PSR KD Rep4; 130C B25 control Rep1; 131N B25 KD Rep1; 131C B25 control Rep2; 132N B25 KD Rep2; B25 control Rep3; 133N B25 KD Rep3; 133C B25 control Rep4; 134N B25 KD Rep4.

After lyophilization, TMT-labeled peptides were redissolved in 200 μL of aqueous 20 mM Ammonium Formate, (pH 10.0). The high pH reversed phase liquid chromatography (bRPLC) separation was performed on a XBridge 4.6 mm x 100 mm column packed with BEH C18 resin,

Supplementary Figures and Legends

3.5 µm particle size, 130 Å pore size (Waters). bRPLC Solvent A was aqueous 2% ACN with 5 mM Ammonium Formate, pH 10.0. Peptides were eluted by: 5% bRPLC B (aqueous 90% acetonitrile with 5 mM Ammonium Formate, pH 10.0) for 10 minutes, 5% - 15% B in 5 minutes, 15-40% B in 47 minutes, 40-100% B in 5 minutes and 100% B held for 10 minutes, followed by re-equilibration at 1% B. The flow rate was 0.6 ml/min, and 12 concatenated fractions were collected. Vacuum centrifugation (Speedvac, Thermo) dried the samples. TMT-labeled peptides were re-dissolved in immobilized metal affinity chromatography (IMAC) loading buffer containing aqueous 0.1% TFA and 85% acetonitrile. Phosphopeptides were enriched using IMAC resin (Cell Signaling Technology # 20432) on a Kingfisher (Thermo). IMAC resin was washed with loading buffer. Peptides were incubated with 10 µL of resin for 30 minutes at room temperature with gentle agitation. The IMAC resin was washed twice with loading buffer followed by wash buffer (aqueous 80% ACN, 0.1% TFA). Phosphopeptides were eluted with aqueous 50% ACN, 2.5% Ammonia. The volume was reduced to 20 µl via vacuum centrifugation.

A nanoflow ultra-high performance liquid chromatograph and nanoelectrospray orbitrap mass spectrometer (RSLCnano and Q Exactive HF-X, Thermo) were used for LC-MS/MS. The sample was loaded onto a pre-column (C18 PepMap100, 2 cm length x 100 µm ID packed with C18 reversed-phase resin, 5 µm particle size, 100 Å pore size) and washed for 8 minutes with aqueous 2% acetonitrile and 0.1% formic acid. Trapped peptides were eluted onto the analytical column, (C18 PepMap100, 25 cm length x 75 µm ID, 2 µm particle size, 100 Å pore size, Thermo). A 120-minute gradient was programmed as: 95% solvent A (aqueous 2% acetonitrile + 0.1% formic acid) for 8 minutes, solvent B (aqueous 90% acetonitrile + 0.1% formic acid) from 5% to 38.5% in 90 minutes, then solvent B from 50% to 90% B in 7 minutes and held at 90% for 5 minutes, followed by solvent B from 90% to 5% in 1 minute and re-equilibration for 10 minutes using a flow rate of 300 nl/min. Spray voltage was 1900 V. Capillary temperature was 275 °C. S lens RF level was set at 40. Top 20 tandem mass spectra were collected in a data-dependent manner. The resolution for MS and MS/MS were set at 60,000 and 45,000 respectively. Dynamic exclusion was 15 seconds for previously sampled peaks.

MaxQuant[5] (version 1.6.14.0) was used to identify peptides using the UniProt human database (March 2020) and quantify the TMT reporter ion intensities. Up to 2 missed trypsin cleavages were allowed. The mass tolerance was 20 ppm first search and 4.5 ppm main search. Reporter ion mass tolerance was set to 0.003 Da. Minimal Precursor intensity fraction 0.75. Carbamidomethyl cysteine was set as fixed modification. Phosphorylation on Serine/Threonine/Tyrosine and Methionine oxidation were set as variable modifications. Both peptide spectral match (PSM) and protein false discovery rate (FDR) were set at 0.05. Match

Supplementary Figures and Legends

between runs feature was activated to carry identifications across samples. For data upload to PRIDE/ProteomeXchange, similar database searches were performed with Mascot (www.matrixscience.com) in Proteome Discoverer (Thermo). Perseus[6] (version 2.0.3.1) was used to perform quality control, log2 transformations, imputation, median subtraction and z-score normalization, annotation, and statistical analyses. T-tests were performed with a permutation-based false discovery rate (FDR <0.01). Kinase and phosphatase activity inference was calculated using the ROKAI explorer[7].

Statistical analysis

Quantified data are represented as mean with SD when applicable. For statistical analyses of any two treatment groups, Student t test was applied. For statistical analyses of three groups or more, one-way ANOVA with Bonferroni correction was performed in Prism version 9. Differences were considered significant if P < 0.05 (*). Increasing levels of significance are denoted by asterisks (** P<0.01, *** P<0.001 **** P<0.0001 or n.s., not significant).

Supp Figure 1

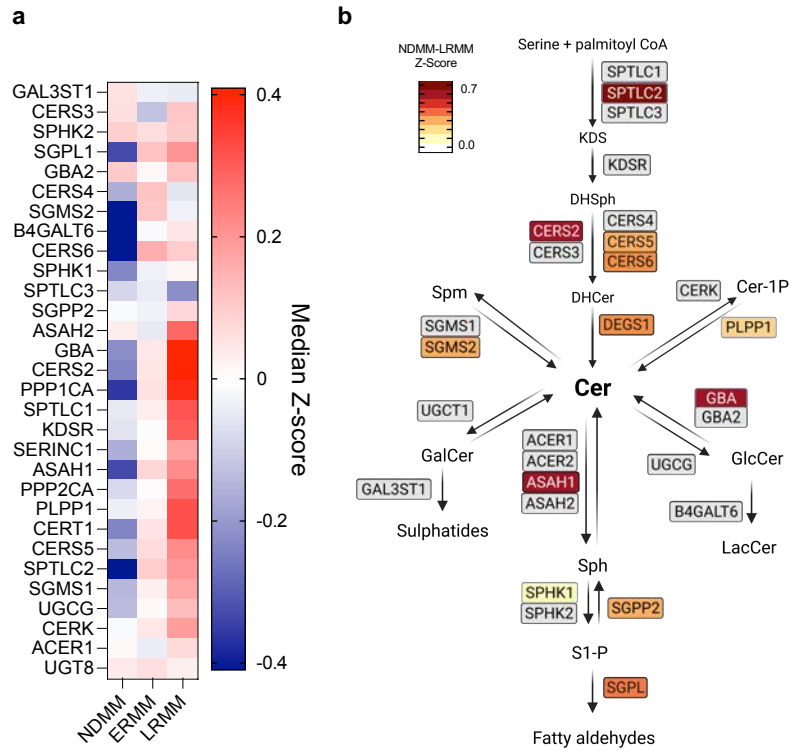

Supplementary Figures and Legends

Supplementary Figure 1. Sphingolipid metabolism is elevated in relapsed/refractory multiple myeloma.

a. showing median mRNA z-score for 30 sphingolipid genes in newly diagnosed (NDMM; n=187), early relapse multiple myeloma (ERMM; n=303) and late relapse multiple myeloma (LRMM, n=182) patients.

b. Diagram of genes involved in the metabolism of sphingolipids. Genes with no significant differences in expression shown in gray boxes. Genes that were significantly enriched in both ERMM and LRMM patients compared to NDMM are colored. Colors represent difference between NDMM and LRMM median z-scores for each gene (LRMM-NDMM) as shown by the color bar in the upper left of the panel.

Supplementary Figures and Legends

Supp Figure 2

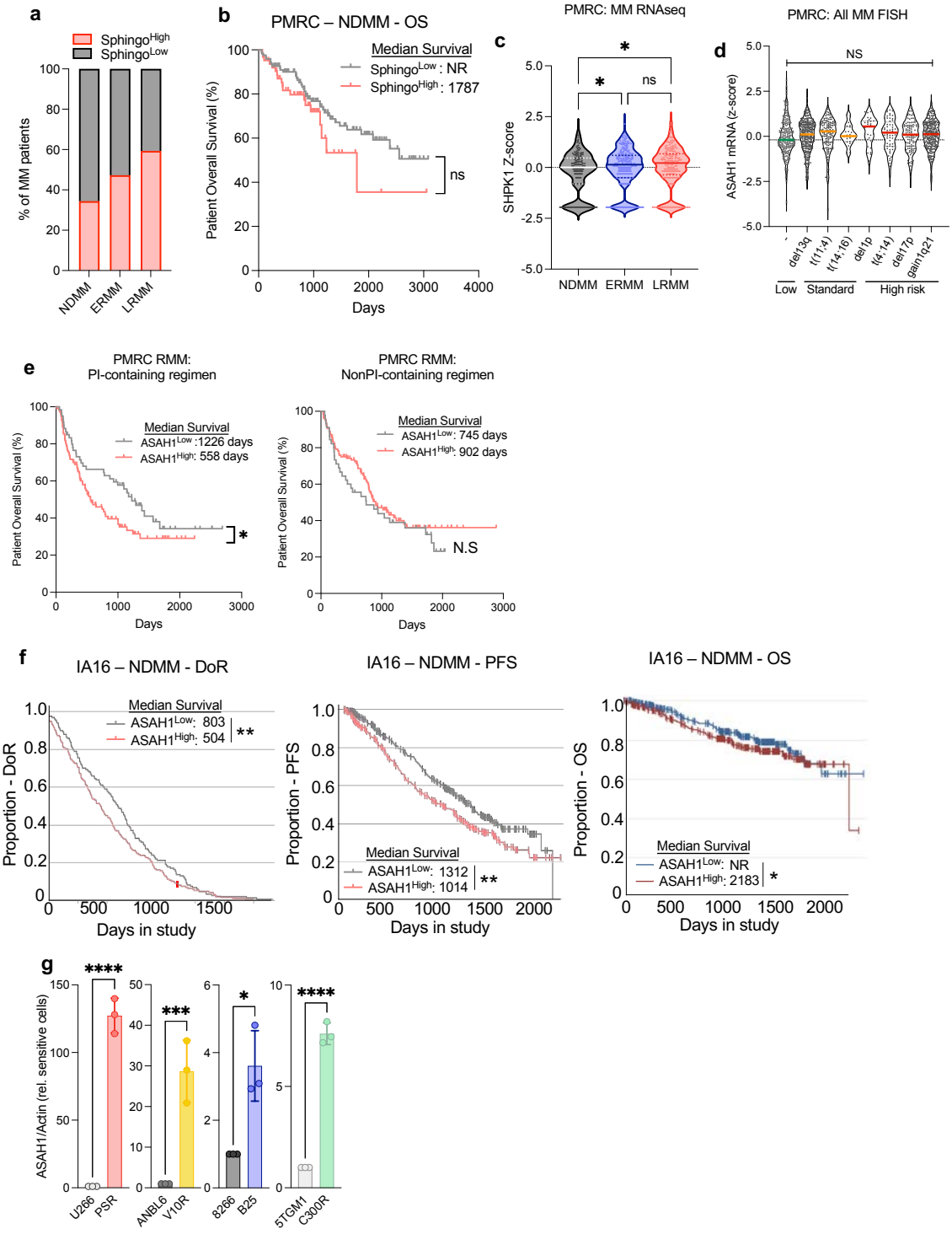

Supplementary Figures and Legends

Supplementary Figure 2. ASAH1 is elevated in relapsed/refractory multiple myeloma and correlates with reduced survival times

a. Percentage of patients in Sphingo^{Low} and Sphingo^{High} clusters in NDMM (n=187), ERMM (n=303) and LRMM (n=182).

b. Kaplan-Meier plot of overall survival NDMM patients in Sphingo^{Low} (n=113) and Sphingo^{High} (n=74) clusters. Inset indicates median survival in days. NR = median survival not reached.

c. Violin plot showing expression of SPHK1 in NDMM (n=187), ERMM (n=303) and LRMM (n=182). Dots represent individual patients.

d. Violin plots showing expression of ASAH1 in all MM patients with no risk factors (-, n= 231) or t(11;4) (n=144), t(14;16) (n=23), t(4;14) (n=64), del1p (n=30) , del13q (n=311), del17p (n=113), gain1q21 (n=293) cytogenetic risk factors.

e. Kaplan-Meier plots of overall survival of ASAH1^{Low} (gray) and ASAH1^{High} (pink) ERMM and LRMM patients treated with proteasome inhibitor-based regimens and non-proteasome inhibitor-based regimens. Inset indicates median survival in days. Kaplan-Meier plots of duration of response (DoR; left), progression free survival (PFS; center) and overall survival (OS; right) of ASAH1^{Low} (gray) and ASAH1^{High} (pink) MM patients in CoMMpass IA16. Inset indicates median survival in days. NR = median survival not reached.

f. Bar chart of normalized ASAH1 protein abundance (ASAH1/actin) in PI resistant MM cells (PSR, V10-R, B25, C300R) relative to their respective PI-sensitive counterparts (U266, ANBL-6, 8226, 5TGM1). Values are mean ± SD of three independent experiments.

Supplementary Figures and Legends

Statistical significance was derived by Log-rank (Mantel-Cox) test (**b, e, f**) and ordinary one-way ANOVA with Dunnett's multiple comparisons test (**c, d, g**). p values of <0.05, <0.01, <0.001 and <0.0001 are represented by *, **, *** and **** respectively. Lines indicate statistical comparisons.

Supplementary Figures and Legends

Supp Figure 3

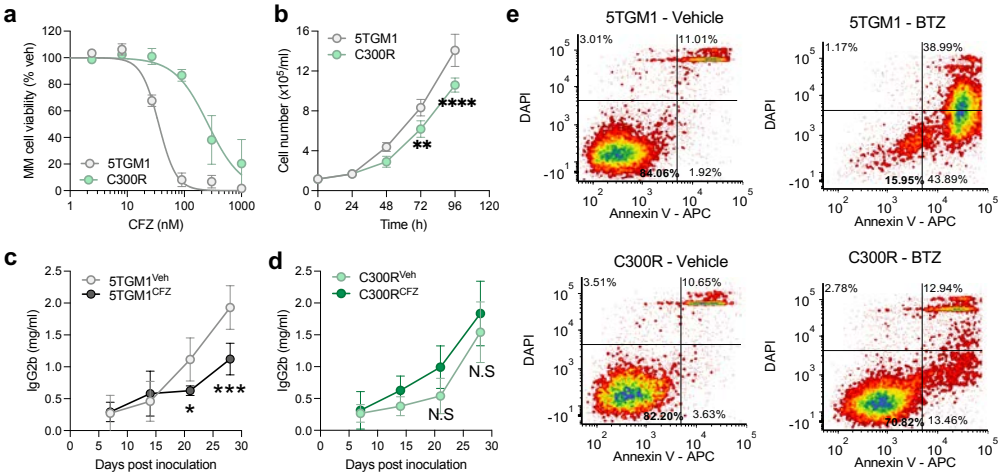

Supplementary Figure 3. Characterization of proteasome inhibitor resistant C300R cells.

a. Dose-response of parental 5TGM1 (gray) and derived PI-resistant C300R (green) myeloma cell lines with carfilzomib (CFZ) after 24 hours as assessed by MTS assay.

b. Growth of 5TGM1 and C300R *in vitro* over 96 hours.

c. Growth and response to twice-weekly carfilzomib (2 mg/kg i.v., consecutive days) or vehicle of parental 5TGM1 in C57Bl6/KalRwrij mice (n=5/group) as measured by serum IgG2b levels.

d. Growth and response to twice-weekly carfilzomib (2 mg/kg i.v., consecutive days) or vehicle of PI-resistant C300R in C57Bl6/KalRwrij mice (n=5/group) as measured by serum IgG2b levels.

e. Density plots showing levels of apoptosis (Annexin-V/DAPI) of 5TGM1 (top row) and C300R (bottom row) treated with vehicle (0.1% DMSO; left) or 10nM BTZ (right) for 24 hours.

Supplementary Figures and Legends

Statistical significance was derived by Ordinary one-way ANOVA with Dunnett's multiple comparisons test (**b**, **c, d**). p values of <0.05, <0.01, <0.001 and <0.0001 are represented by *, **, *** and **** respectively.

Supplementary Figures and Legends

Supp Figure 4

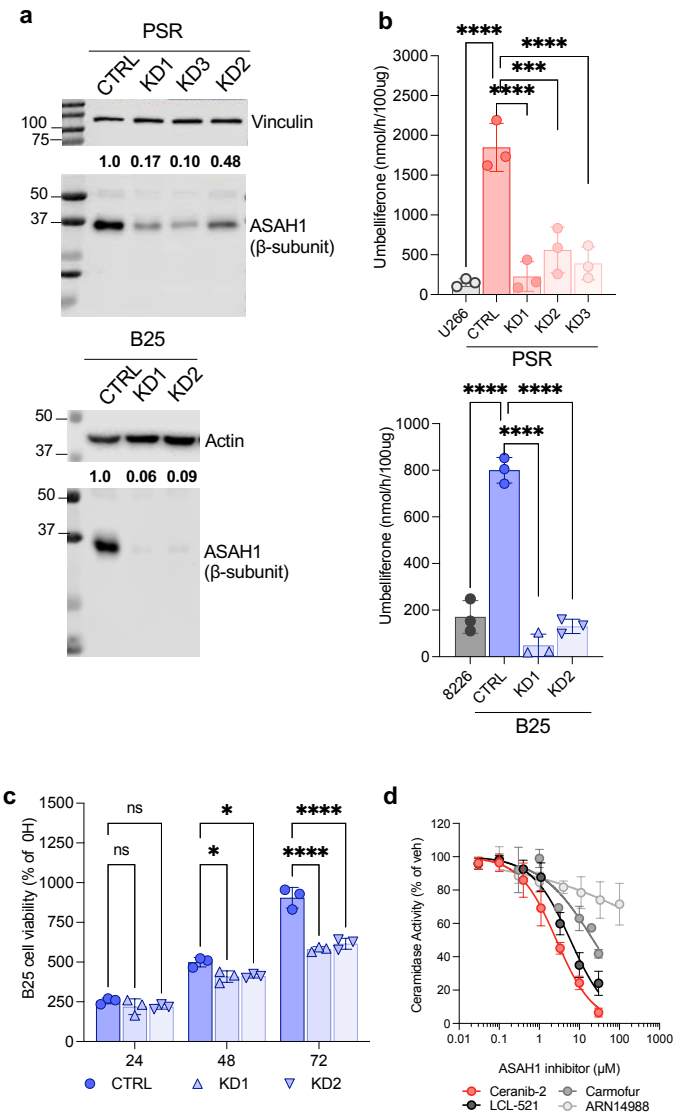

Supplementary Figure 4. Inhibition of ASAH1 reduces ASAH1 activity and cell viability in relapsed/refractory multiple myeloma cell lines.

a. Representative Immunoblots of ASAH1 and vinculin expression in PSR (top blot) nontargeting shRNA (CTRL) and ASAH1 shRNA knockdown cells (KD1-3). Emboldened values represent the normalized ASAH1 (ASAH1/vinculin) relative to the

non-targeting control MM cells. Representative Immunoblot of ASAH1 and actin expression in B25 (bottom blot) nontargeting shRNA (CTRL) and ASAH1 shRNA knockdown cells (KD1-2). Emboldened values represent the normalized ASAH1 (ASAH1/Actin) relative to the non-targeting control B25 cells.

b. Bar chart of ASAH1 activity as assayed by umbelliferone release from RBM14-C12 in PI sensitive U266 and PI resistant PSR (top) and PI sensitive 8226 and PI resistant B25 (bottom) MM cells with non-targeting shRNA (CTRL) or ASAH1 knockdown (KD1-3).

c. Bar chart of growth of control (CTRL) and ASAH1 knockdown (KD1/2) B25 MM cells as assessed by MTS at indicated time points.

d. Dose-response of ASAH1 enzymatic activity in PSR cells after 3 hours incubation in ASAH1 inhibitors at indicated concentrations.

Statistical significance was derived by Ordinary one-way ANOVA with Dunnett's multiple comparisons test (**b**, **c**). p values of <0.05, <0.001 and <0.0001 are represented by *, *** and **** respectively.

Supplementary Figures and Legends

Supp Figure 5

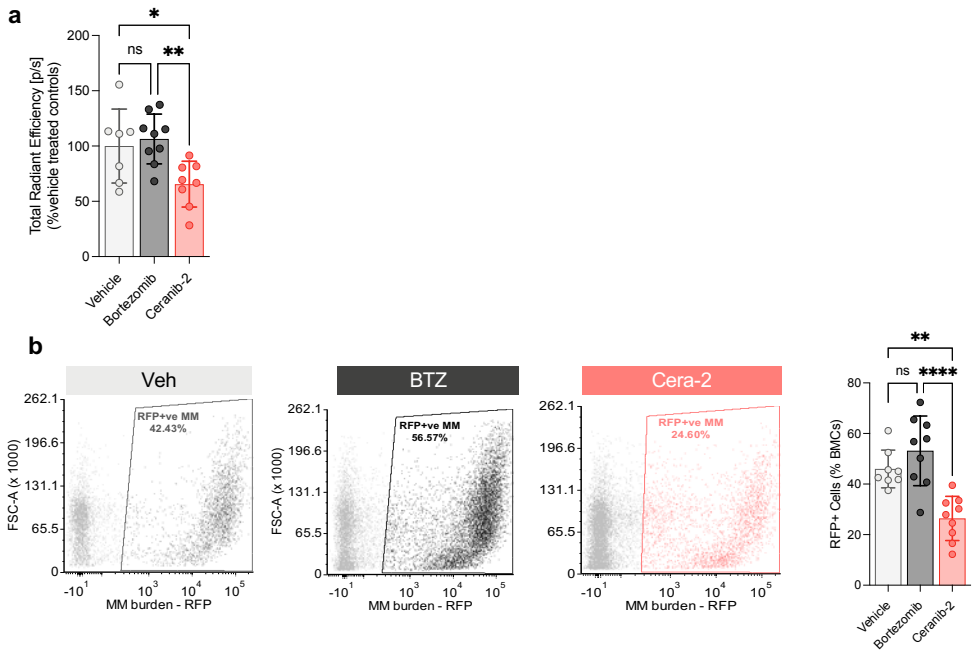

Supplementary Figure 5. Treatment of relapsed/refractory multiple myeloma-bearing mice with ceranib-2 reduces tumor burden and suppresses osteolytic bone disease in mice.

a. Bar chart of total radiant efficiency of mice in treated Cera-2 (n=8), BTZ (n=9), or vehicle (n=7) at the final time point in study including all mice normalized to the mean of the vehicle treated mice

b. Representative scatter plots of RFP+ Myeloma cells in bone marrow of mice in vehicle, bortezomib and ceranib-2 treated groups at end point (left). Quantification of the number of RFP+ MM cells as a percentage of live cells in the bones of mice treated with vehicle (n=7), bortezomib (n=9) or ceranib-2 (n=8) at end point.

Supplementary Figures and Legends

Statistical significance was derived by Ordinary one-way ANOVA with Dunnett's multiple comparisons test (**a**, **b**). p values of <0.05, <0.01 and <0.0001 are represented by *, ** and **** respectively. N.S = not significant.

Supplementary Figures and Legends

Supp Figure 6

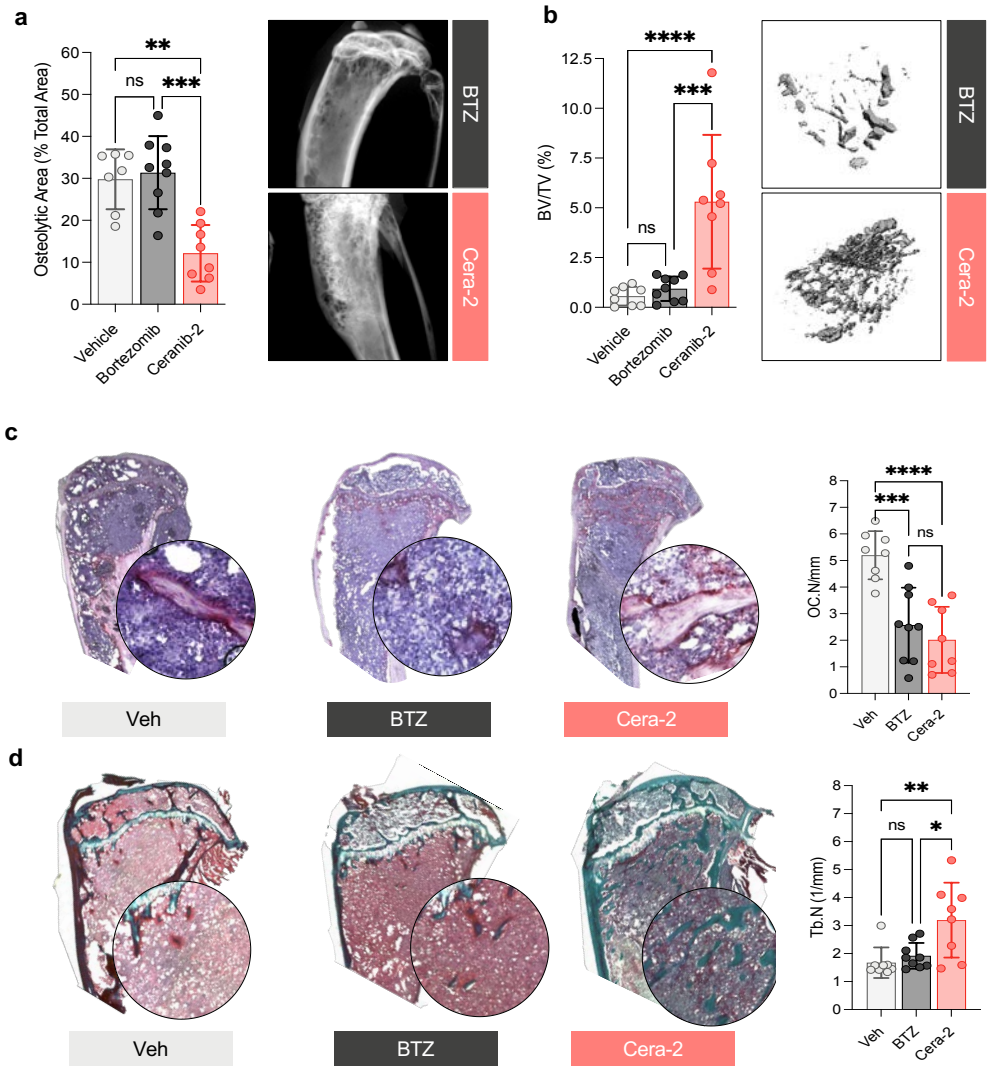

Supplementary Figure 6. Treatment of relapsed/refractory multiple myeloma-bearing mice with ceranib-2 suppresses osteolytic bone disease in mice

a. Bar chart quantification (left) of osteolytic area as a percentage of total bone area in tibia of mice treated with vehicle (n=7), ceranib-2 (n=8), or bortezomib (n=9) at

Supplementary Figures and Legends

endpoint. Representative x-ray images of bortezomib and ceranib-2 treated mice (right).

b. Bar chart (left) of trabecular bone volume as a percentage of tissue volume in tibia of mice treated with vehicle (n=7), ceranib-2 (n=8), or bortezomib (n=9) at endpoint. Representative μCT images (right) of osteolysis in bortezomib and ceranib-2 treated mice.

c. Representative micrographs (4X magnification; left) of TRAcP stained tibiae from mice in vehicle (n=7), ceranib-2 (n=8), or bortezomib (n=9) treated groups at end point. Inset = 20X. Bar chart (right) of osteoclast numbers per mm of bone surface in the trabecular of tibiae from mice in vehicle (n=7), ceranib-2 (n=8), or bortezomib (n=9) treated groups at end point.

d. Representative micrographs (4X magnification; left) of trichrome stained tibiae in vehicle, bortezomib and ceranib-2 treated groups at end point. Inset = 20X. Bar chart (right) of trabecular number in tibiae of mice in vehicle (n=7), ceranib-2 (n=8), or bortezomib (n=9) treated groups at end point as measured by microCT.

Statistical significance was derived by Ordinary one-way ANOVA with Dunnett's multiple comparisons test (**a**, **b**). p values of <0.05, <0.01, p<0.001 and <0.0001 are represented by *, **, *** and **** respectively. N.S = not significant. Lines indicate the statistical comparison.

Supplementary Figures and Legends

Supp Figure 7

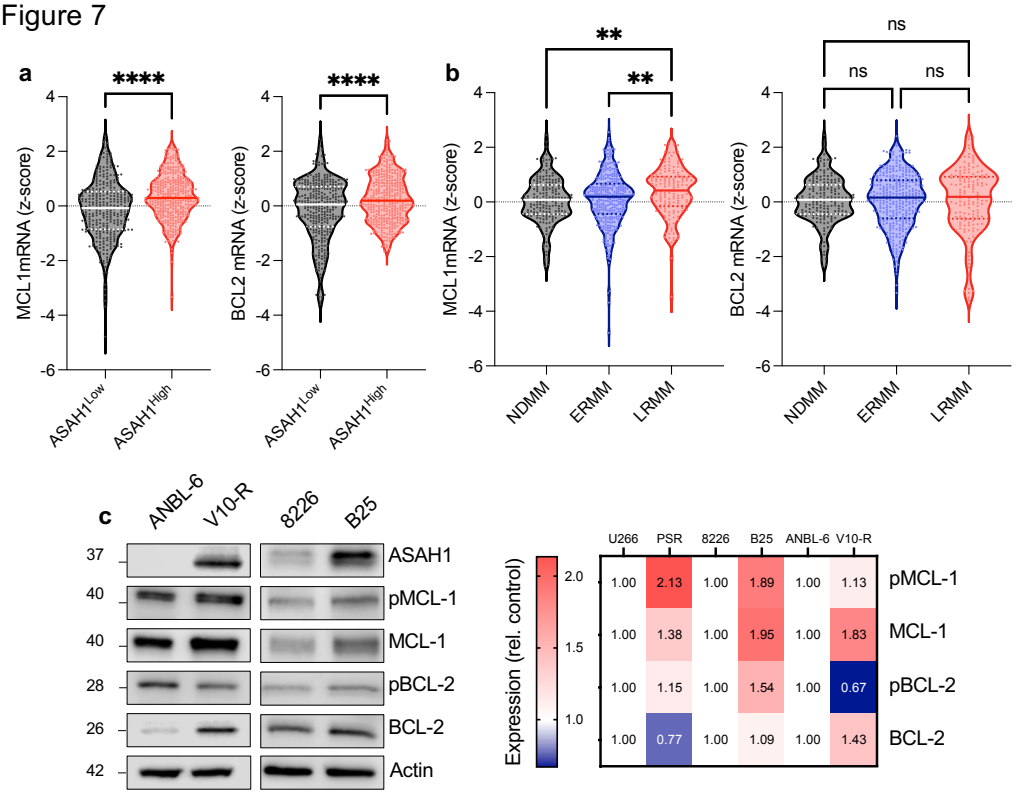

Supplementary Figure 7. ASAH1 is associated with MCL-1 and BCL-2 levels in relapsed/refractory multiple myeloma.

a. Violin plot of MCL1 mRNA expression (left) in ASAH1^{Low} (gray; n=323) ASAH1^{High} (pink n=349) Pentecost Myeloma Research Center (PMRC) multiple myeloma (MM) patients. Violin plot BCL2 mRNA expression (right) in ASAH1^{Low} (gray; n=321) ASAH1^{High} (pink n=351).

b. Violin plot of MCL1 and BCL2 mRNA expression (Z-score) in newly diagnosed multiple myeloma (NDMM, n=187), early relapse multiple myeloma (ERMM, n=303) and late relapse multiple myeloma (LRMM, n=182) PMRC patients.

Supplementary Figures and Legends

c. Immunoblot of ASAH1, pMCL-1 (T163), total MCL-1, p-BCL-2 (S70), and total BCL-2 expression in PI-sensitive (ANBL6, 8226) and PI-resistant (V10-R, B25) MM cells. Heatmap showing the mean house-keeping protein normalized expression of pMCL-1 (T163), total MCL-1, p-BCL-2 (S70), and total BCL-2 expression relative to PI-sensitive controls in PI-sensitive (U266, ANBL6, 8226) and PI-resistant (PSR, V10-R, B25) MM cells. Values are mean ± SD of at least two independent experiments. Statistical significance was derived by unpaired t -test (**a**) or ordinary one-way ANOVA with Dunnett's multiple comparisons test (**b**). p values of <0.01 and <0.0001 are represented by ** and **** respectively. N.S = not significant. Lines indicate the statistical comparison.

Supplementary Figures and Legends

Supp Figure 8

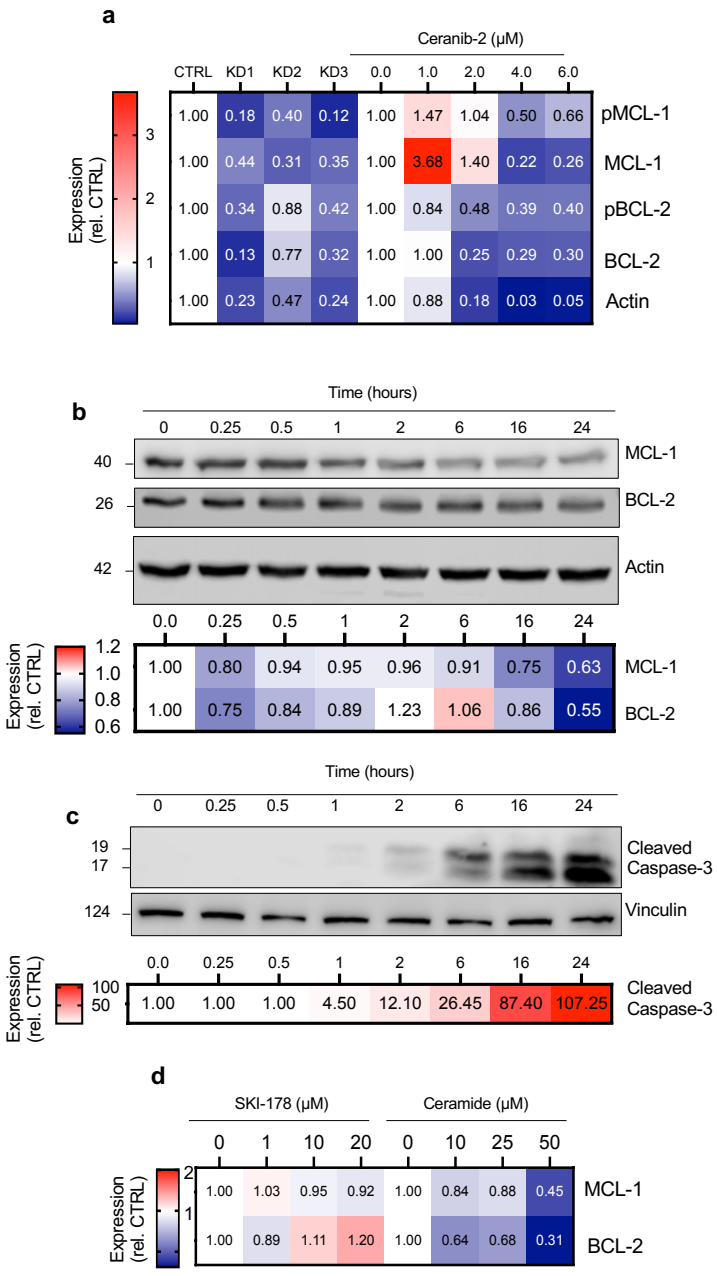

Supplementary Figure 8. ASAH1 is associated with MCL-1 and BCL-2 levels in relapsed/refractory multiple myeloma.

Supplementary Figures and Legends

a. Heatmap showing the mean normalized expression of ASAH1, pMCL-1 (T163), total MCL-1, p-BCL-2 (S70), and total BCL-2 expression in control (CTRL) or ASAH1 knockdown (KD1-3) PSR multiple myeloma (MM) cells or PSR MM cells treated with 2 μM ceranib-2 for indicated number of hours, relative to either CTRL or vehicle treated PSR cells. Values are mean of two independent experiments.

b. Immunoblot (top) of total MCL-1 and total BCL-2 expression in PI-resistant V10-R MM cells treated with 5 μM ceranib-2 and 1 ng/mL IL-6 at indicated times post treatment. Heatmap (bottom) showing the mean normalized expression of total MCL-1 and total BCL-2 expression in V10-R cells in response to 5 μM ceranib-2. Values are mean of two independent experiments

c. Immunoblot (top) of cleaved caspase-3 expression in PI-resistant V10-R MM cells treated with 5 μM ceranib-2 and 1 ng/mL IL-6 at indicated times post treatment. Heatmap (bottom) showing the mean normalized expression of cleaved caspase-3 expression in V10-R cells in response to 5 μM ceranib-2. Values are mean of two independent experiments

d. Heatmap showing the mean normalized expression of total MCL-1 and total BCL-2 expression in PSR MM cells treated with indicated concentrations of sphingosine kinase inhibitor SKI-178 or ceramide C6 for 4 hours. Values are mean of two independent experiments

Supplementary Figures and Legends

Supp Figure 9

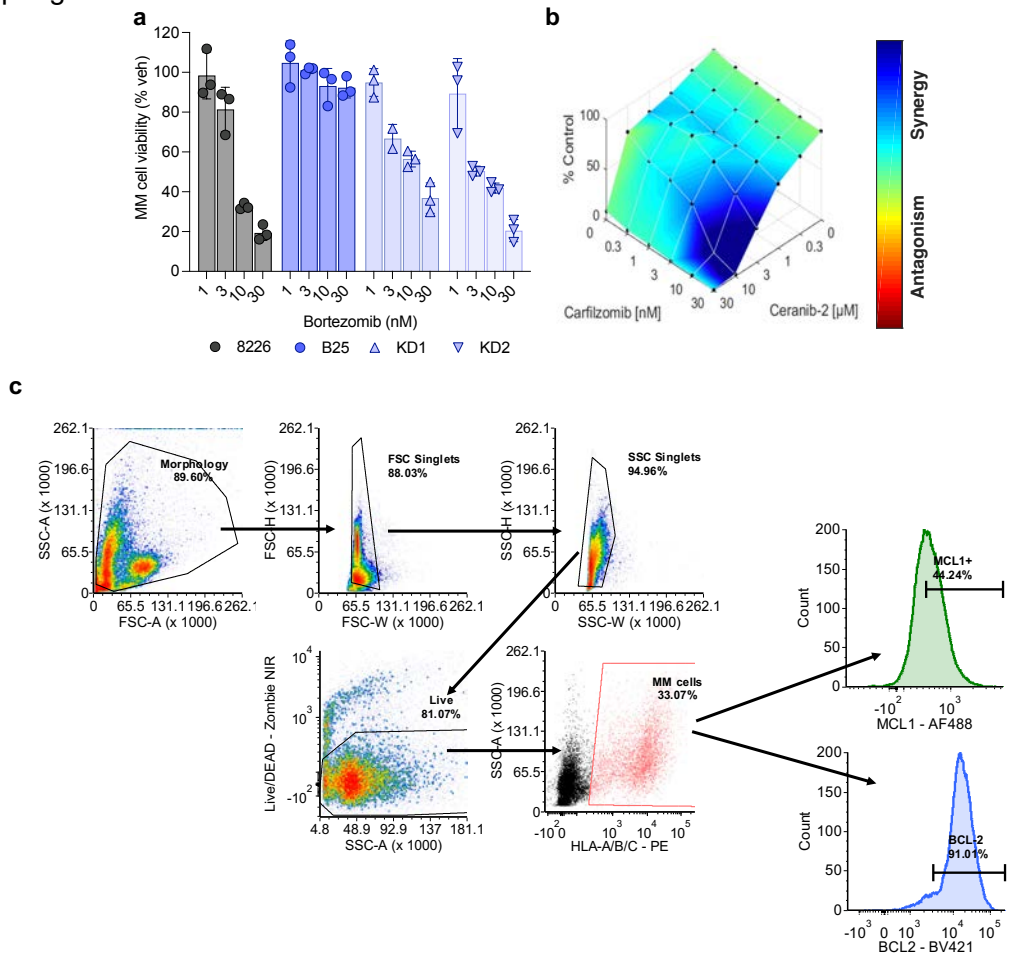

Supplementary Figure 9. Inhibition of ASAH1 restores PI-sensitivity in relapsed/refractory multiple myeloma cell lines.

a. Bar chart showing the effect of indicated concentrations of BTZ on 8226, CTRL (B25) and ASAH1 KD (KD1/2) B25 cell viability after 24 hours as assessed by MTS assay.

b. LOEWE synergy plot showing the effect of indicated concentrations of ceranib-2 and carfilzomib as single agents and in combination on C300R murine MM cells after 24 hours as assessed by MTS assay.

Supplementary Figures and Legends

c. Flow cytometry gating strategy for identification of HLA A/B/C+ MCL-1+ and BCL2+ MM cells in the bone marrow of mice *ex vivo* studies in Figure **4**.

Supplementary Figures and Legends

Supp Figure 10

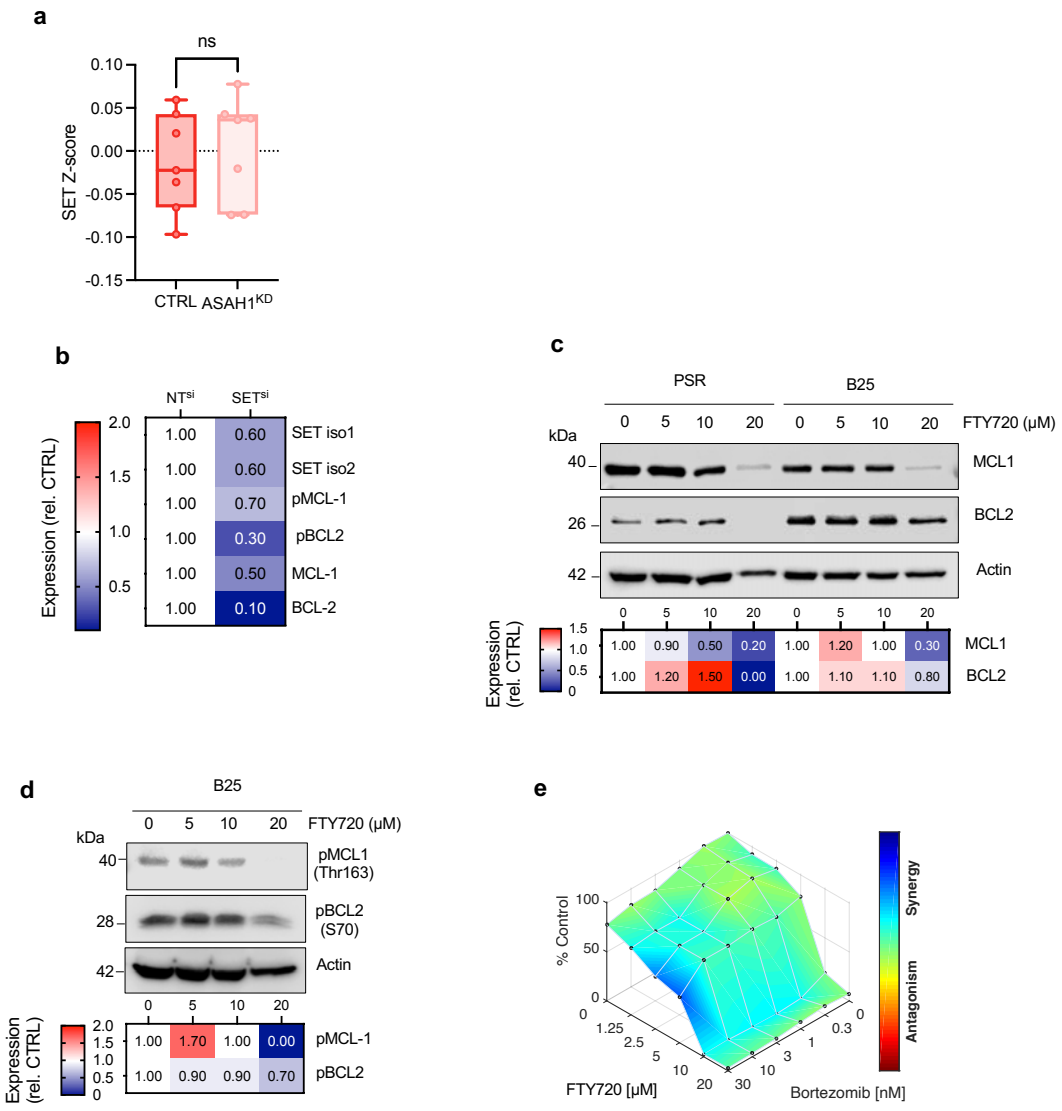

Supplementary Figure 10. SET is associated with relapse and resistance to proteasome inhibitors in relapsed/refractory multiple myeloma.

a. Box and whisker plot of SET expression (normalized Z-score) in CTRL and ASAH1 KD PI resistant multiple myeloma (MM) cells quantitated by LC-MS/MS proteomics. Each dot represents a biological replicate (n=7/group).

Supplementary Figures and Legends

b. Heatmap quantification of protein expression of SET isoforms 1 and 2, total and phosphorylated MCL-1 and BCL-2 48 hours following transfection of PSR cells with non-targeting siRNA (NTsi) or SET-targeting siRNA (SETsi) normalized to housekeeping protein relative to non-targeting siRNA (NTsi) controls. Values are mean of 3 independent experiments.

c. Immunoblot (top) of MCL1, BCL2 and actin following treatment with indicated concentration of FTY-720 (4 hours) in PI-resistant MM cell lysates. Heatmap quantification (bottom) of protein expression normalized to housekeeping protein relative to vehicle treated controls. Values are mean of 3 independent experiments.

d. Immunoblot (top) of phosphorylated MCL1 (Thr163), phosphorylated BCL2 (S70) and actin following treatment with indicated concentration of FTY-720 (4 hours) in PI-resistant MM cell lysates. Heatmap quantification (bottom) of protein expression normalized to housekeeping protein relative to vehicle treated controls.

e. LOEWE synergy plot of the viability of PSR MM cells 24 hours after treatment with indicated concentrations of FTY-720 and BTZ.

Statistical significance was derived by unpaired t -test (**a**). N.S = not significant.

Supplementary Figures and Legends

Supp Figure 11

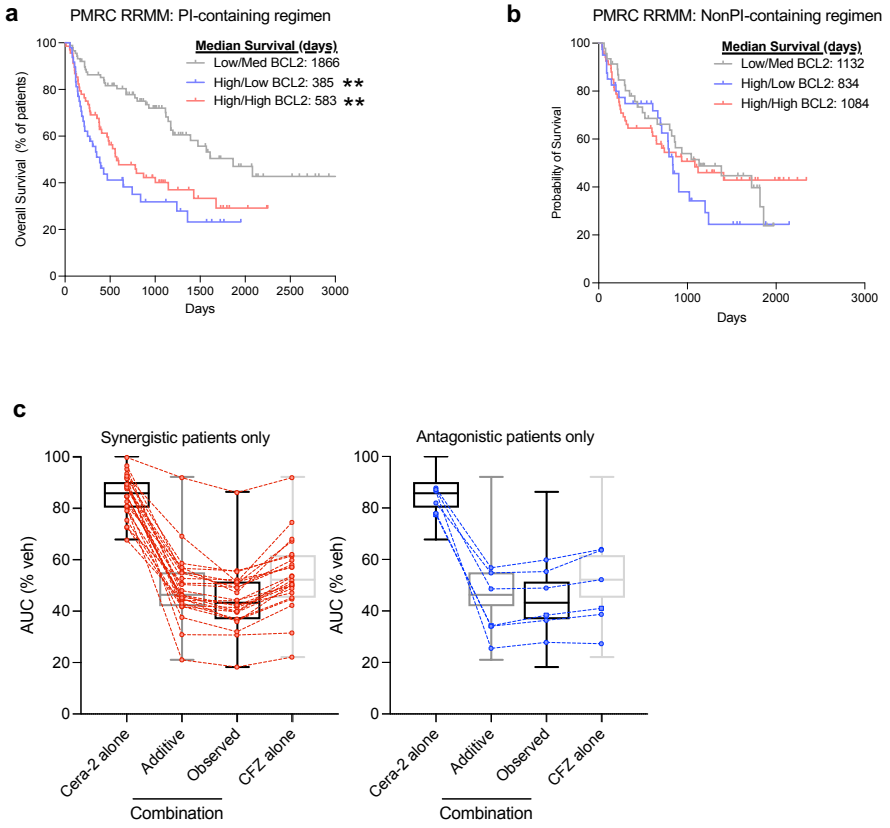

Supplementary Figure 11. Ceranib-2 synergizes with carfilzomib in most *ex vivo* multiple myeloma patient samples.

a. Kaplan-Meier plot of overall survival of relapsed/refractory multiple myeloma (RRMM) patients treated with PI-containing regimen in each cluster. Low/Med BCL-2 (gray), High/Low BCL-2 (blue), High/High BCL-2 (pink). Inset indicates median survival in days.

b. Kaplan-Meier plot of overall survival of relapsed/refractory multiple myeloma (RRMM) patients treated with NonPI-containing regimen in each cluster. Low/Med BCL-2 (gray), High/Low BCL-2 (blue), High/High BCL-2 (pink). Inset indicates median survival in days

Supplementary Figures and Legends

c. Box and whisker plot showing the median AUC of 30 patients' (1 smoldering multiple myeloma (SMOL), 1 plasma cell leukemia (PCL), 14 newly diagnosed multiple myeloma (NDMM) and 14 relapsed/refractory multiple myeloma (RRMM) patients' response *ex vivo* to single agent ceranib-2 (cera-2), carfilzomib (CFZ), or the combination – either additive or observed. Additive represents the expected value of combining two agents whereas observed indicates the actual response. The difference between additive and observed values is used to calculate either synergy or antagonism. Red dots and lines represent synergy (left plot, n=24) whereas blue lines and dots represents antagonism (right plot, n=6).

Statistical significance was derived by Log-rank (Mantel-Cox) test (**a, b**). p values of <0.01 are represented by ** and denote statistical difference to Low/Med BCL2 group.

Supplementary Figures and Legends

References

1. Chen S, Dai Y, Pei XY, et al. CDK inhibitors upregulate BH3-only proteins to sensitize human myeloma cells to BH3 mimetic therapies. Cancer Res. 2012;72(16):4225-4237.
2. Chen S, Zhang Y, Zhou L, et al. A Bim-targeting strategy overcomes adaptive bortezomib resistance in myeloma through a novel link between autophagy and apoptosis. Blood, 2014:2687-2697.
3. Zhuang J, Shirazi F, Singh RK, et al. Ubiquitin-activating enzyme inhibition induces an unfolded protein response and overcomes drug resistance in myeloma. Blood. 2019;133(14):1572-1584.
4. Silva A, Jacobson T, Meads M, Distler A, Shain K. An Organotypic High Throughput System for Characterization of Drug Sensitivity of Primary Multiple Myeloma Cells. Jove-J Vis Exp. 2015;101):
5. Cox J, Mann M. MaxQuant enables high peptide identification rates, individualized p.p.b.-range mass accuracies and proteome-wide protein quantification. Nat Biotechnol. 2008;26(12):1367-1372.
6. Tyanova S, Temu T, Sinitcyn P, et al. The Perseus computational platform for comprehensive analysis of (prote)omics data. Nat Methods. 2016;13(9):731-740.
7. Yilmaz S, Ayati M, Schlatzer D, Cicek AE, Chance MR, Koyuturk M. Robust inference of kinase activity using functional networks. Nat Commun. 2021;12(1):1177.

Supplementary Figures and Legends